

## Climate Variability and Radiocarbon in the CM2Mc Earth System Model

ERIC D. GALBRAITH,\* EUN YOUNG KWON,<sup>+</sup> ANAND GNANADESIKAN,<sup>#</sup> KEITH B. RODGERS,<sup>+</sup>  
STEPHEN M. GRIFFIES,<sup>#</sup> DANIELE BIANCHI,<sup>+</sup> JORGE L. SARMIENTO,<sup>+</sup> JOHN P. DUNNE,<sup>#</sup>  
JENNIFER SIMEON,<sup>@</sup> RICHARD D. SLATER,<sup>+</sup> ANDREW T. WITTENBERG,<sup>#</sup> AND ISAAC M. HELD<sup>#</sup>

\* *Department of Earth and Planetary Science, McGill University, Montreal, Quebec, Canada*

<sup>+</sup> *Princeton University, Princeton, New Jersey*

<sup>#</sup> *Geophysical Fluid Dynamics Laboratory, Princeton, New Jersey*

<sup>@</sup> *Laboratoire des Sciences du Climat et l'Environnement, Gif-sur-Yvette, France*

(Manuscript received 28 June 2010, in final form 15 February 2011)

### ABSTRACT

The distribution of radiocarbon ( $^{14}\text{C}$ ) in the ocean and atmosphere has fluctuated on time scales ranging from seasons to millennia. It is thought that these fluctuations partly reflect variability in the climate system, offering a rich potential source of information to help understand mechanisms of past climate change. Here, a long simulation with a new, coupled model is used to explore the mechanisms that redistribute  $^{14}\text{C}$  within the earth system on interannual to centennial time scales. The model, the Geophysical Fluid Dynamics Laboratory Climate Model version 2 (GFDL CM2) with Modular Ocean Model version 4p1 (MOM4p1) at coarse-resolution (CM2Mc), is a lower-resolution version of the Geophysical Fluid Dynamics Laboratory's CM2M model, uses no flux adjustments, and is run here with a simple prognostic ocean biogeochemistry model including  $^{14}\text{C}$ . The atmospheric  $^{14}\text{C}$  and radiative boundary conditions are held constant so that the oceanic distribution of  $^{14}\text{C}$  is only a function of internal climate variability. The simulation displays previously described relationships between tropical sea surface  $^{14}\text{C}$  and the model equivalents of the El Niño–Southern Oscillation and Indonesian Throughflow. Sea surface  $^{14}\text{C}$  variability also arises from fluctuations in the circulations of the subarctic Pacific and Southern Ocean, including North Pacific decadal variability and episodic ventilation events in the Weddell Sea that are reminiscent of the Weddell Polynya of 1974–76. Interannual variability in the air–sea balance of  $^{14}\text{C}$  is dominated by exchange within the belt of intense “Southern Westerly” winds, rather than at the convective locations where the surface  $^{14}\text{C}$  is most variable. Despite significant interannual variability, the simulated impact on air–sea exchange is an order of magnitude smaller than the recorded atmospheric  $^{14}\text{C}$  variability of the past millennium. This result partly reflects the importance of variability in the production rate of  $^{14}\text{C}$  in determining atmospheric  $^{14}\text{C}$  but may also reflect an underestimate of natural climate variability, particularly in the Southern Westerly winds.

### 1. Introduction

One of the great challenges in understanding the ocean's role in climate variability is the scarcity of direct measurements, particularly prior to the last few decades. Such data limitations seriously hinder progress in understanding modes of interannual variability. These modes include the El Niño–Southern Oscillation (ENSO), for which continuous observations of many centuries are required for accurate characterization (Wittenberg 2009;

Vecchi and Wittenberg 2010), and changes in the Southern Ocean overturning and Southern Annular Mode (SAM), which vary on time scales of multiple decades (Visbeck 2009). Proxy data can help to fill this gap, but many proxy measurements are confounded by spurious influences and are difficult to interpret.

Radiocarbon is one such proxy, directly recorded with high fidelity by marine microplankton providing decadal–centennial resolution (Hughen et al. 1998) and in both corals and tree rings at annual or even subannual resolution. Thousands of individual tree-ring records have been spliced together to reconstruct the radiocarbon history of the troposphere in both Northern and Southern Hemispheres (Fig. 1). Meanwhile, long coral records of radiocarbon have been recovered from the tropics (Druffel

---

*Corresponding author address:* Eric D. Galbraith, Dept. of Earth and Planetary Science, McGill University, 3450 University St., Montreal QC H3A 2A7, Canada.  
E-mail: eric.galbraith@mcgill.ca

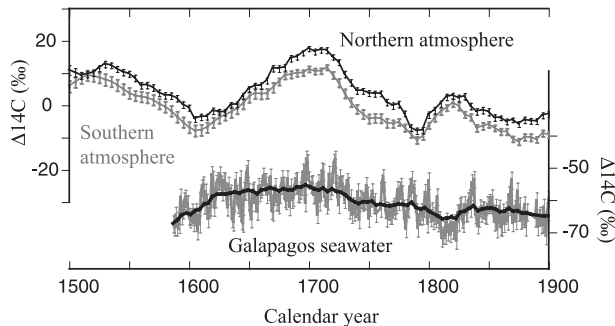


FIG. 1. Observational reconstructions of  $\Delta^{14}\text{C}$  in the atmosphere and ocean: (top profiles) atmospheric  $\Delta^{14}\text{C}$  for the Northern Hemisphere [black, (Reimer et al. 2004)] and the Southern Hemisphere [gray, (McCormack et al. 2004)] over AD 1500–1900, reconstructed from tree ring archives and (bottom) reconstructed  $\Delta^{14}\text{C}$  of surface water at Galapagos, reconstructed from fossil coral (Druffel et al. 2007), measured in annual bands (gray) and smoothed (thick black line). Measurement errors are shown as reported.

1997; Guilderson et al. 1998; Druffel et al. 2004; Fallon and Guilderson 2008; Guilderson et al. 2009), revealing interannual variability in local seawater radiocarbon well in excess of the analytical error associated with coral measurements ( $\sim 3\%$  measurement error, Guilderson et al. 2009). Looking even further back in time, large changes in the radiocarbon activities of the ocean and atmosphere accompanied the warming that occurred at the end of the last ice age (Shackleton et al. 1988; Hughen et al. 1998; Galbraith et al. 2007; Marchitto et al. 2007; Skinner et al. 2010). Unfortunately, the manifold influences on radiocarbon activities can confuse the translation of these geochemical archives to useful climate information.

Radiocarbon is produced in the stratosphere and upper troposphere by cosmic rays, at a rate dependent on the strengths of the geomagnetic field and the solar wind (Masarik and Beer 1999) and decays with a 5730-yr half-life. Radiocarbon is quite well mixed in the atmosphere, with a small interhemispheric gradient (Fig. 1). A small portion of radiocarbon is lost through decay in the terrestrial biosphere, while the majority dissolves in the ocean, at a rate dependent on the ocean state (Siegenthaler et al. 1980). The fact that  $^{14}\text{C}$  production takes place exclusively in the atmosphere, coupled with the long air–sea equilibration time scale of carbon, caused the ocean to be everywhere undersaturated with  $^{14}\text{C}$  under preindustrial conditions, but to varying degrees. The slow pace of deep ocean circulation allows radiogenic decay to significantly deplete the  $^{14}\text{C}$  activity of abyssal waters so that strong undersaturation of  $^{14}\text{C}$  is a clear tracer of these “old” waters where they come to the surface (Toggweiler et al. 1991; Toggweiler and Samuels 1993; Rodgers et al. 2000; Gnanadesikan et al. 2004).

The complexity of interpreting radiocarbon records arises from the fact that both its natural rate of production and its distribution within the earth system could have changed simultaneously (e.g., Broecker and Barker 2007). Variability in the relatively small atmospheric  $^{14}\text{C}$  reservoir over the last millennium (Fig. 1), including “Suess wiggles” with a characteristic time scale of  $\sim 200$  yr (Suess 1968), are frequently argued to reflect changes in the production rate of radiocarbon (Siegenthaler et al. 1980; Stuiver and Quay 1980; Masarik and Beer 1999; Muscheler et al. 2007). At the same time, interannual modes of climate variability are thought to drive redistribution of radiocarbon within the ocean (Rodgers et al. 1997; Rodgers et al. 2004; Druffel et al. 2007), with some impact on air–sea exchange. Meanwhile, sustained changes in ocean circulation, such as those thought to have occurred during the end of the last ice age, are argued to have caused very large changes in the redistribution of radiocarbon between the ocean and atmosphere (Siegenthaler et al. 1980; Hughen et al. 1998; Broecker and Barker 2007). These processes have been variously explored with box models (Siegenthaler et al. 1980), ocean GCMs (Toggweiler et al. 1989; Toggweiler et al. 1991; Rodgers et al. 1997), and ocean models coupled to simplified atmospheres (Meissner et al. 2003; Schmittner 2003). Through such works, radiocarbon has proven a useful diagnostic of the mean ocean circulation (Duffy et al. 1997; Guilderson et al. 2000; Gnanadesikan et al. 2004; Matsumoto et al. 2004; Grumet et al. 2005). However, the relationship between coupled ocean–atmosphere variability and the global distribution of natural radiocarbon on centennial time scales has received little attention.

In this paper we take a broad view of how oceanic radiocarbon is linked to natural, unforced variability in a global coupled climate model with no flux adjustments, but with a fixed atmospheric radiocarbon activity. The model, climate model version 2 with the Modular Ocean Model version 4p1 at coarse resolution (CM2Mc), includes more complex oceanic and atmospheric physics than those used in prior coupled model studies with radiocarbon (Marchal et al. 1999; Meissner et al. 2003; Schmittner 2003; Stocker and Wright 1996). CM2Mc is a new  $3^\circ$  configuration of the Geophysical Fluid Dynamics Laboratory (GFDL) coupled atmosphere–ocean GCM, using code similar to that of CM2.1 (Delworth et al. 2006) but with new parameterizations for subgrid-scale ocean physics and a new ocean biogeochemistry module. The coarse resolution enables us to simulate hundreds of years with many different tracers using reasonable computational resources, while maintaining a relatively realistic solution with robust modes of unforced ocean–atmosphere variability on decadal time

scales. Section 2 describes the radiocarbon model and the mean state simulation produced under preindustrial radiative forcing. Section 3 examines the relationship between simulated modes of climate variability and oceanic radiocarbon at the sea surface. Section 4 discusses how the simulated variability of ocean circulation would modulate the air–sea balance of radiocarbon, applying the disequilibrium flux concept of Rodgers et al. (2011). Section 5 concludes the paper. Two appendices detail the model formulation and the control simulation.

## 2. Radiocarbon simulation

Radiocarbon is simulated as part of the idealized ocean biogeochemistry (iBGC) module, integrated simultaneously with the ocean component of CM2Mc (see appendix A for a complete model description). Dissolved inorganic carbon (DIC), that is, the sum of dissolved  $\text{CO}_2$ ,  $\text{H}_2\text{CO}_3$ ,  $\text{HCO}_3^-$ , and  $\text{CO}_3^{2-}$ , is carried as a prognostic tracer. Air–sea gas exchange follows the Ocean Carbon Model Intercomparison Project (OCMIP2) protocol (Najjar and Orr 1998) and the Wanninkhof (1992) quadratic wind-speed-dependent piston velocity, using salinity to estimate alkalinity (i.e., with no carbonate cycling). Organic carbon, dissolved and particulate, is not carried as an explicit tracer but is linked to the cycling of organic phosphorus through a strict stoichiometric ratio of 106 C:P (Redfield et al. 1963). Dissolved inorganic radiocarbon ( $\text{DI}^{14}\text{C}$ ) is also carried as a prognostic tracer, with a concentration equal to its true concentration multiplied by  $r_{1890}^{12/14}$ , the standard “pre-anthropogenic” atmospheric  $^{12}\text{C}/^{14}\text{C}$  ratio, that is, the ratio preceding contamination by fossil fuel burning and above-ground nuclear weapon testing, defined relative to tree rings from circa AD 1890 (Stuiver and Polach 1977). This multiplication causes the concentrations to be similar to those of DIC, avoiding numerical difficulties.  $\text{DI}^{14}\text{C}$  undergoes the same air–sea exchange processes as DIC but, in contrast to total carbon, its cycling also includes uptake by plankton and export as particulate organic  $^{14}\text{C}$ , as well as partitioning of uptake into a dissolved organic  $^{14}\text{C}$  tracer,  $\text{DO}^{14}\text{C}$ . The  $\Delta^{14}\text{C}$  (see Stuiver and Polach 1977 for the definition of this quantity) in equilibrium with the atmosphere is prescribed (equal to 0‰ in the simulations shown here), and the half-life for decay is 5730 yr.

The physical model was initialized from observed temperature and salinity, with the ocean at rest and integrated for 1000 years. Following this, the biogeochemical model was initialized from observed phosphate, DIC and  $\text{DI}^{14}\text{C}$ , and integrated for 1000 years using preindustrial boundary conditions. The latter 500 years of this run are presented here. Note that radiocarbon is not fully equilibrated:

the global average  $\Delta^{14}\text{C}$  gradually increases in the ocean throughout this interval (by  $1.1\text{‰ century}^{-1}$ ), including a surface  $\Delta^{14}\text{C}$  increase of  $0.3\text{‰ century}^{-1}$ . Linear trends are removed from the 500-yr time series in all statistical analyses.

The sea surface radiocarbon simulation is difficult to evaluate precisely, given that almost all available observations were made after massive contamination of surface waters by above-ground nuclear weapons testing in the 1950s and early 1960s. Chemistry-based regression estimates of the prebomb radiocarbon activities are available (Rubin and Key 2002), but these are less reliable in surface waters and do not correct for the invasion of  $^{14}\text{C}$ -depleted  $\text{CO}_2$  emissions from fossil fuel burning (Suess 1953). A comparison of the model simulation to the Global Ocean Data Analysis Project (GLODAP) regression-based product shows similar large-scale surface  $\Delta^{14}\text{C}$  patterns, with simulated  $\Delta^{14}\text{C}$  values generally higher in the model (Fig. 2). The higher model  $\Delta^{14}\text{C}$  is largely attributable to the lack of correction for fossil-fuel carbon but may also reflect air–sea exchange errors. At the same time, the  $\Delta^{14}\text{C}$  in tropical upwelling regions is lower than expected from the coral-based preindustrial estimates, summarized in Toggweiler and Samuels (1993), which could reflect excessive vertical mixing across the tropical thermocline.

The distribution of radiocarbon in the ocean interior, isolated from the fossil fuel effect, agrees better with estimates of natural radiocarbon but highlights circulation error biases also apparent in the phosphate simulation (see Fig. B5). Within the Atlantic, the water mass structure is well reproduced, while in the Pacific, weak stratification of the upper ocean allows excessive ventilation from above (Fig. 2). Both the overactive North Pacific ventilation and excessive vertical mixing across the thermocline would contribute to the general overestimate of radiocarbon activities in the deep Pacific Ocean. Basinwide averages of deep ocean  $\Delta^{14}\text{C}$ , calculated according to Matsumoto et al. (2004) for the final 20 years of the simulation, lie within the error of the available observational data, as shown in Table B1. However, there is an ongoing drift to higher (more radiogenic) values, consistent with excessive ventilation of the deep ocean, that would likely cause these errors to be larger when equilibrated.

## 3. Variability of sea surface radiocarbon

We analyze the temporal variability of  $\Delta^{14}\text{C}$  at the ocean surface by dividing the globe into three regions: tropics, northern extratropics, and southern extratropics. Empirical orthogonal functions (EOFs) are calculated from deseasonalized monthly anomalies of surface  $\Delta^{14}\text{C}$

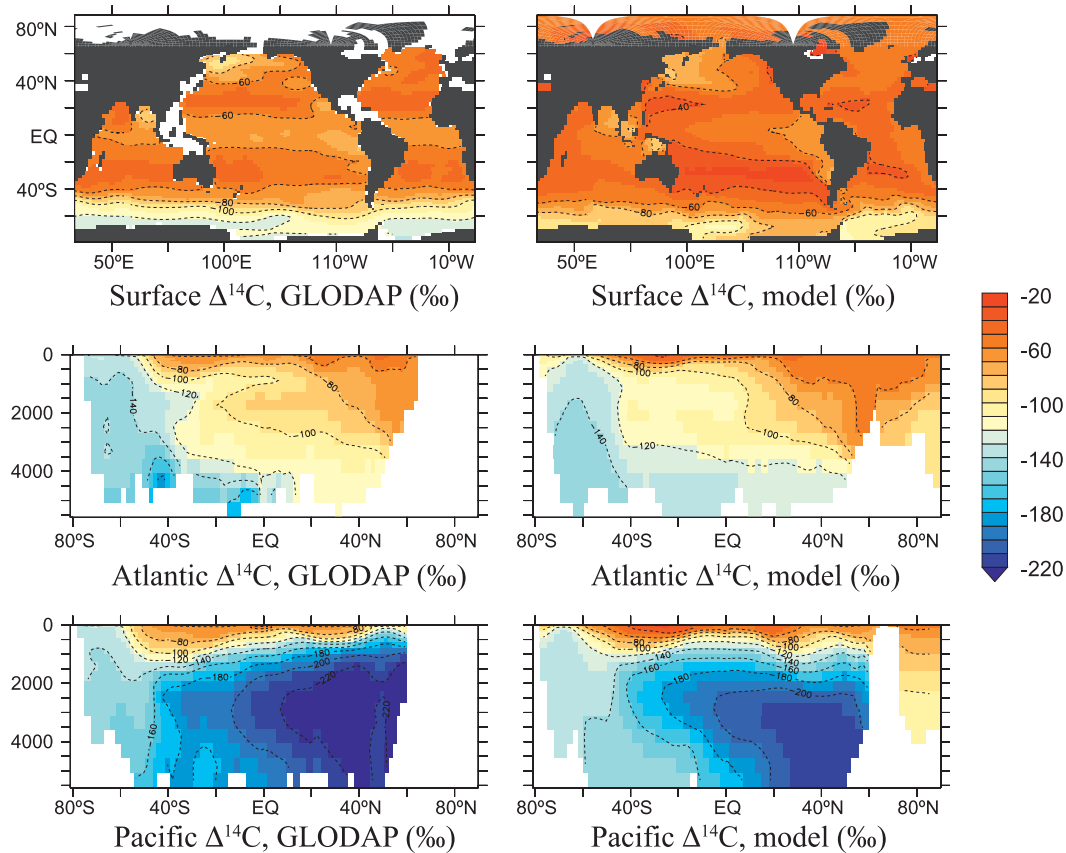


FIG. 2. Radiocarbon simulation in the ocean of CM2Mc: (left) the GLODAP “background”  $\Delta^{14}\text{C}$  activities for which the prebomb (circa 1950) activity is estimated by a calibrated alkalinity regression (Key et al. 2004) and (right) the corresponding model output. (top) The ocean surface; strong regional variability in the model may reveal small-scale circulation features lost in the heavily smoothed observation-based regression, while the generally lower activities in the data product are largely attributable to the prebomb invasion of radiocarbon-depleted fossil-fuel carbon. Zonally-averaged vertical sections are presented for (middle) the Atlantic and (bottom) the Pacific basins.

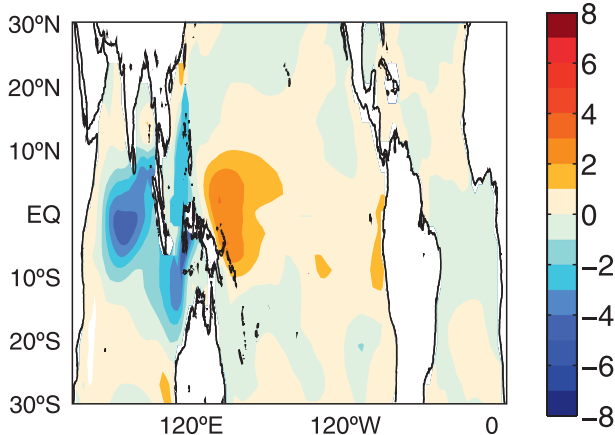


FIG. 3. Leading EOF of surface  $\Delta^{14}\text{C}$  variability in the tropics. This EOF accounts for 69% of the variance and is linked to lateral advective processes that are associated with changes in the warm pool structure (Rodgers et al. 1997). The deseasonalized monthly

anomaly of surface  $\Delta^{14}\text{C}$  is taken from the last 100 years of simulations for the EOF analysis. The EOF pattern is scaled such that the corresponding principal component time series has a standard deviation of one.

*a. Tropics*

The first EOF of tropical surface seawater  $\Delta^{14}\text{C}$  shows a dipole between the eastern equatorial Indian Ocean and the western equatorial Pacific (Fig. 3). This EOF accounts for 69% of the variability and is linked to the dynamics of the west Pacific warm pool.

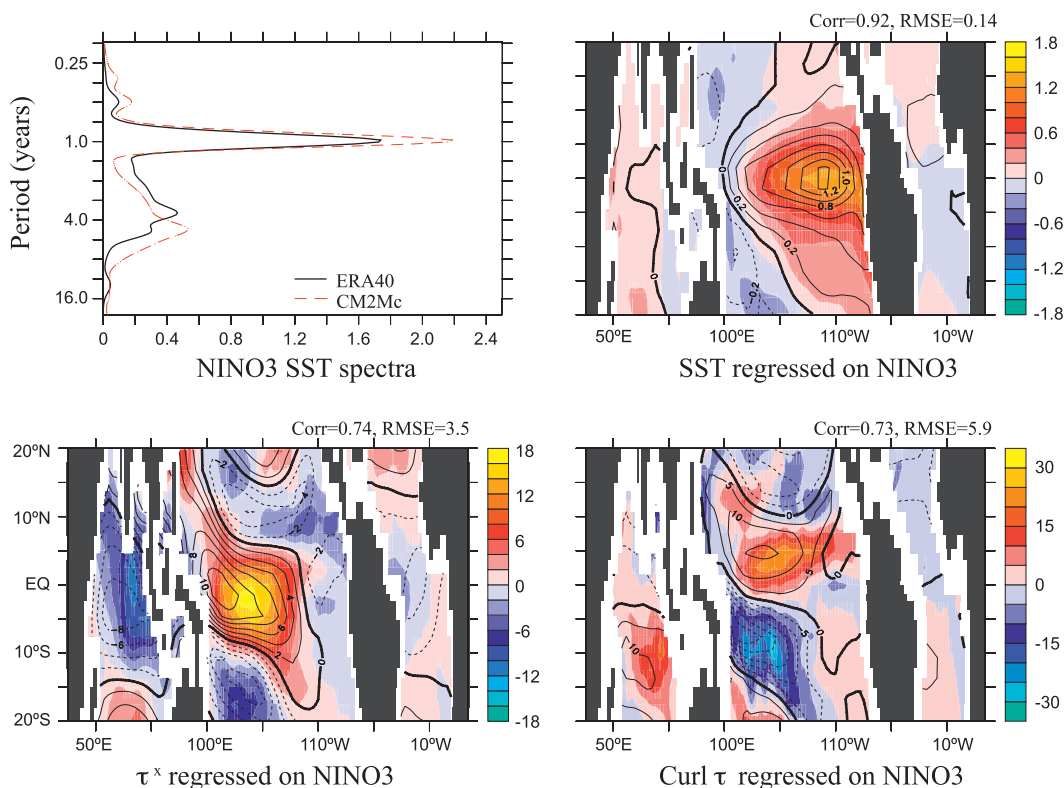


FIG. 4. Simulation of unforced ENSO-like variability: (top left) frequency spectrum ( $^{\circ}\text{C}^2 \text{ octave}^{-1}$ ) of SST in the Niño-3 region, reanalysis (ERA-40, black) and CM2Mc (red, dashed). (top right) Regression of SST anomalies on Niño-3 SST, reanalysis (ERA-40, colors) and CM2Mc (contours). (bottom left) As in top right, showing zonal wind stress anomalies on the ocean ( $\text{N m}^{-2}$ ). (bottom right) As in top right, showing wind stress curl anomalies ( $\text{N m}^{-3}$ ).

Modeled interannual variability of SST in the tropics is dominated by a structure similar to ENSO. The SST anomaly in the Niño-3 region (Fig. 4, top left), has an annual peak that is somewhat larger than observed, while the interannual peak is roughly the right size but shifted toward slightly lower frequency. This small degree of disagreement between  $\sim 50$  years of data and 500 years of model output may not be significant, given the pronounced heterogeneity of ENSO over interdecadal and centennial time scales in models and, presumably, the real world (Wittenberg 2009). The structure of the warm anomaly is also very similar to observations (Fig. 4, top right) with a correlation coefficient of 0.92, though the zero line is shifted to the west slightly. The wind stress anomaly (Fig. 4, bottom left) resulting from this temperature anomaly has about the right magnitude but is also shifted to the west while the wind stress curl anomaly is also about the right magnitude though shifted slightly to the north. In addition, the lagged regression of global SST monthly anomalies onto the Niño-3 index is structurally very similar between the model and observations (the first and second columns of Fig. 5).

The structural similarity suggests that the unforced model ENSO variability is operating via similar large-scale mechanisms to those underlying true ENSO variability, which can be monitored by SST within the Niño-3 region. The third column of Fig. 5 shows the regression coefficients of the monthly  $\Delta^{14}\text{C}$  anomaly onto the Niño-3 SST anomaly. The El Niño phase of ENSO, characterized by a high Niño-3 SST anomaly (Fig. 5, zero lag), is well correlated with positive anomalies of surface  $\Delta^{14}\text{C}$  in the western equatorial Pacific Ocean. The correlation arises from a weakening of the easterly winds during El Niño events, which reduces the upwelling of  $^{14}\text{C}$ -depleted subsurface waters in the central and eastern equatorial Pacific (Toggweiler et al. 1991). As a result of the reduced zonal gradient of surface  $\Delta^{14}\text{C}$  combined with a weakening of the equatorial counter currents, eastward advection of  $^{14}\text{C}$ -rich waters becomes reduced in the western equatorial Pacific. Consequently, the western pool of  $^{14}\text{C}$ -enriched surface waters intensifies and expands eastward, resulting in a net accumulation of high- $\Delta^{14}\text{C}$  waters in the western and central equatorial Pacific Ocean, as previously shown by Rodgers et al. (1997).

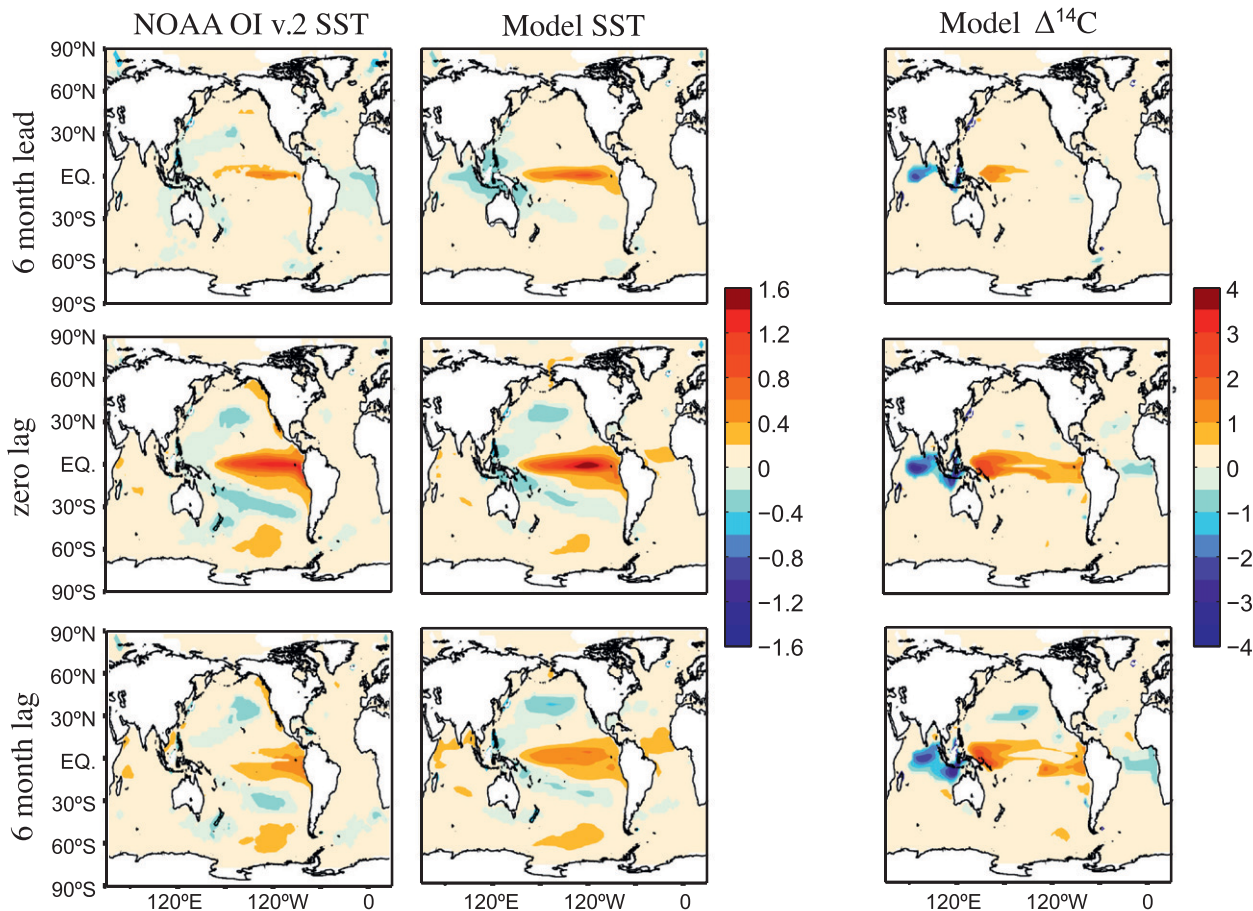


FIG. 5. Phasing between Niño-3 SST and temperature or  $\Delta^{14}\text{C}$  at the sea surface: (top) 6-month lead correlations between the indicated variable and Niño-3 SST, (middle) in-phase correlations, and (bottom) 6-month lag correlations. The regressions of (left) observed SST (Reynolds et al. 2002), (middle) the corresponding regressions for model SST, and (right) the regressions for model  $\Delta^{14}\text{C}$ . The regression patterns indicate SST and  $\Delta^{14}\text{C}$  change in association with one standard deviation increase in the Niño-3 SST. Deseasonalized monthly anomalies for (left) 27 yr and (middle and right) 100 yr are used in the regressions. Values that are significant at (left) 90% and at (middle and right) 99% are plotted.

Meanwhile, the transport of Pacific waters by the Indonesian Throughflow has a large impact on the surface  $\Delta^{14}\text{C}$  of the eastern Indian Ocean. Illustrating this, the linear correlation of  $\Delta^{14}\text{C}$  near Lombok Strait ( $11^{\circ}\text{S}$ ,  $115^{\circ}\text{W}$ ) with the volume transport of the Indonesian Throughflow is  $r = 0.69$  with a slope of  $\sim 2\text{‰ Sv}^{-1}$  ( $\text{Sv} \equiv 10^6 \text{ m}^3 \text{ s}^{-1}$ ). A large part of the Indonesian Throughflow variability is related to reduced transport during El Niño events ( $\sim 10 \text{ Sv}$  rather than  $\sim 14 \text{ Sv}$ ) which restricts the supply of  $^{14}\text{C}$ -rich waters from the Pacific warm pool and results in the negative correlation shown in Fig. 5 for the eastern Indian Ocean (right column). Reduced Indonesian Throughflow transport during El Niño events has also been well documented by observations (Tillinger and Gordon 2009). However, the correlation of the  $\Delta^{14}\text{C}$  near Lombok Strait with Niño-3 SST ( $r = 0.55$ ) is less than with the Indonesian Throughflow itself since the throughflow responds to more than just

ENSO. Therefore, the  $\Delta^{14}\text{C}$  of the eastern Indian Ocean also reflects these additional sources of Indonesian Throughflow variability, as well as local changes in circulation.

We note that the response pattern of  $\Delta^{14}\text{C}$  to ENSO is different from that of SST to ENSO in two distinctive ways (Fig. 5, compare middle and right columns). While the SST response is characterized by an out of phase relationship between the tropical and extratropical Pacific, the  $\Delta^{14}\text{C}$  response is dominated by a zonal contrast between the tropical Pacific and Indian Oceans, part of which reflects the change in the strength of the Indonesian Throughflow. In addition, the  $\Delta^{14}\text{C}$  response persists with very little alteration at a 6-month lag, unlike the SST signal which has largely decayed by this point. This persistence reflects the long air–sea equilibration time of  $\Delta^{14}\text{C}$  in seawater ( $\sim 10 \text{ yr}$ ), allowing it to maintain a more distinct memory of ocean circulation

changes: as a result, the ENSO signal persists throughout an entire year, providing ample opportunity for it to be recorded in corals (Druffel 1997).

### b. Northern Hemisphere

Interannual variability of surface seawater  $\Delta^{14}\text{C}$  in the Northern Hemisphere is dominated by the subarctic Pacific, which displays two distinct patterns (Fig. 6). The first EOF is centered on the Aleutian Islands and accounts for 36% of the variance. The second EOF reveals a dipole, with opposing poles in the Gulf of Alaska and western subarctic Pacific, accounting for 19% of the variance. Both EOF patterns are evident in subsurface waters to a depth of  $\sim 300$  m.

The North Pacific has a circulation bias that includes an erroneously low-latitude position of the Oyashio extension, a weak Alaskan stream, an underexpression of the western subarctic gyre, and excessive ventilation to intermediate depths. Given these biases in the simulated mean state, the simulated variability must be viewed with caution.

The two leading EOFs of surface  $\Delta^{14}\text{C}$  reflect a basinwide propagating mode. The first EOF leads the second by  $\sim 4$  yr (correlation coefficient of 0.55) while the second EOF leads the first by  $\sim 13$  yr (correlation coefficient of 0.46). Basinwide decreases of surface  $\Delta^{14}\text{C}$  (the first EOF) occur with weaker subpolar gyre circulation. This EOF correlates with anomalous eastward flow of the upper-ocean currents north of  $40^\circ\text{N}$  and reduced exchange with the subtropical gyre (Fig. 7). This results in anomalous advection of  $^{14}\text{C}$ -depleted waters from the northwest Pacific basin to the northeast Pacific, reducing the zonal gradient. In addition, increased mixed layer depths occur in the northwestern edges of the Bering Sea. Entrainment of  $^{14}\text{C}$ -depleted subsurface waters into the mixed layer contributes to the basinwide reduction of surface  $\Delta^{14}\text{C}$ .

In contrast, the second EOF of the surface  $\Delta^{14}\text{C}$  anomaly is well correlated with a strengthening of westerly winds over the Kuroshio Extension region. Enhanced wind stress curl over the subpolar gyre intensifies the gyre circulation (Fig. 7), resulting in anomalous southward flow of  $^{14}\text{C}$ -depleted surface waters in the western subarctic gyre and anomalous northward flow of  $^{14}\text{C}$ -rich subtropical water on the eastern side. This increases the zonal contrast of surface  $\Delta^{14}\text{C}$  in the subpolar North Pacific.

The time series for the second leading EOF of surface  $\Delta^{14}\text{C}$  anomaly correlates weakly ( $r = 0.14$ , 95% significance) with the Arctic Oscillation (AO) index (the simulation of which is shown in Fig. B4) owing to its dependence on the westerly winds. Meanwhile a less weak correlation ( $r = -0.35$ , 95% significance) occurs between the second EOF and the Pacific decadal

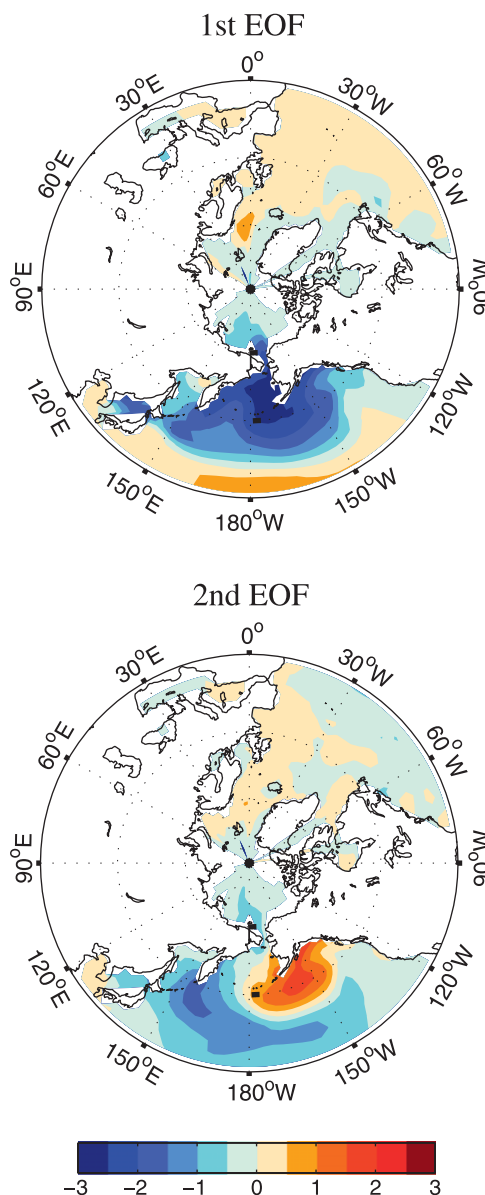


FIG. 6. First and second leading EOFs of surface  $\Delta^{14}\text{C}$  in the northern extratropics, accounting for 36% and 19% of the variance, respectively; EOFs calculated as in Fig. 3.

oscillation time series (Mantua et al. 1997). The first EOF is similarly correlated with the Pacific decadal oscillation, but with the opposite sign ( $r = 0.33$ , 95% significance), while it shows no relationship with the Arctic Oscillation, given its less direct dependence on the westerly winds.

### c. Southern Hemisphere

The first EOF of sea surface  $\Delta^{14}\text{C}$  in the Southern Hemisphere extratropics has the largest amplitude of anywhere in the ocean (Fig. 8). This variability is

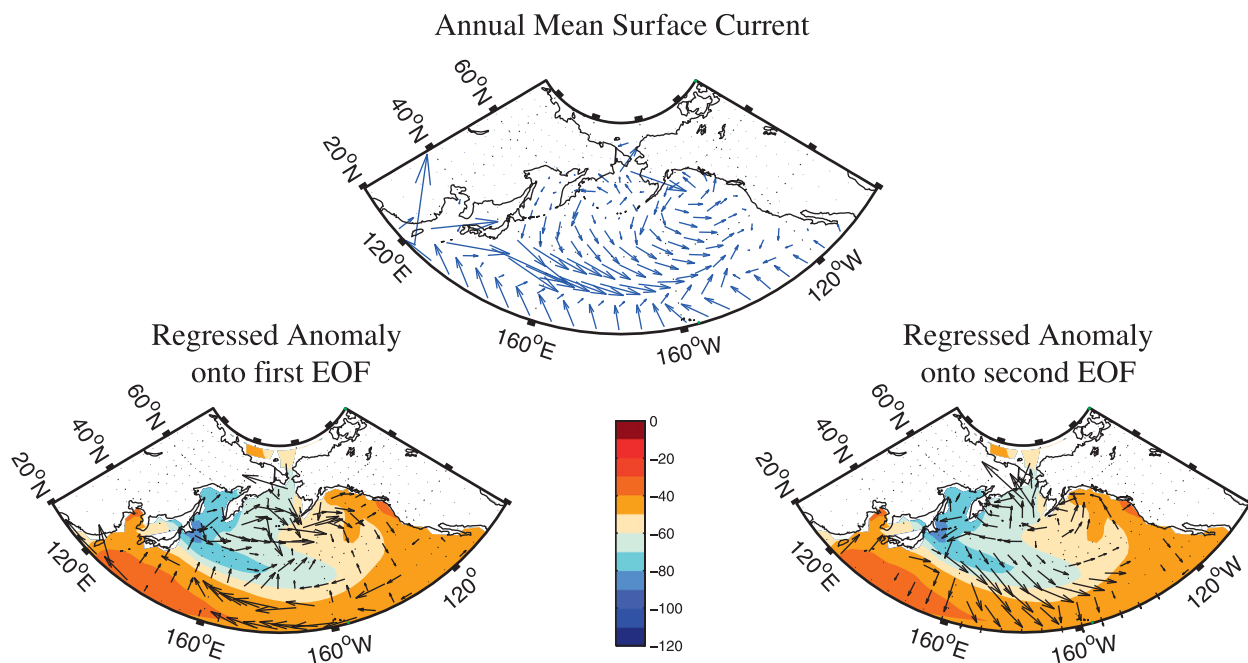


FIG. 7. (top) Annual mean surface currents in the North Pacific and (bottom) surface flow anomaly regressed on to the first and second EOFs of the  $\Delta^{14}\text{C}$  variability. The velocity vectors in the bottom panels are scaled by 30 relative to the top panel, significant at the 90% level. Color shade represents the annual mean  $\Delta^{14}\text{C}$  at the surface.

focused within the Weddell Sea. The second EOF is likely part of a propagating mode, of which a main standing mode is represented by the first EOF. The third EOF is much weaker.

In assessing the causes underlying this sea surface  $\Delta^{14}\text{C}$  variability, we consider first the Southern Annular

Mode (SAM), a dominant pattern of climate variability over the Southern Ocean on interannual to decadal time scales. The SAM is characterized by meridional fluctuations of air masses south of  $20^{\circ}\text{S}$ , associated with changes in sea level pressure and the location and intensity of the Southern Hemisphere westerlies (e.g.,

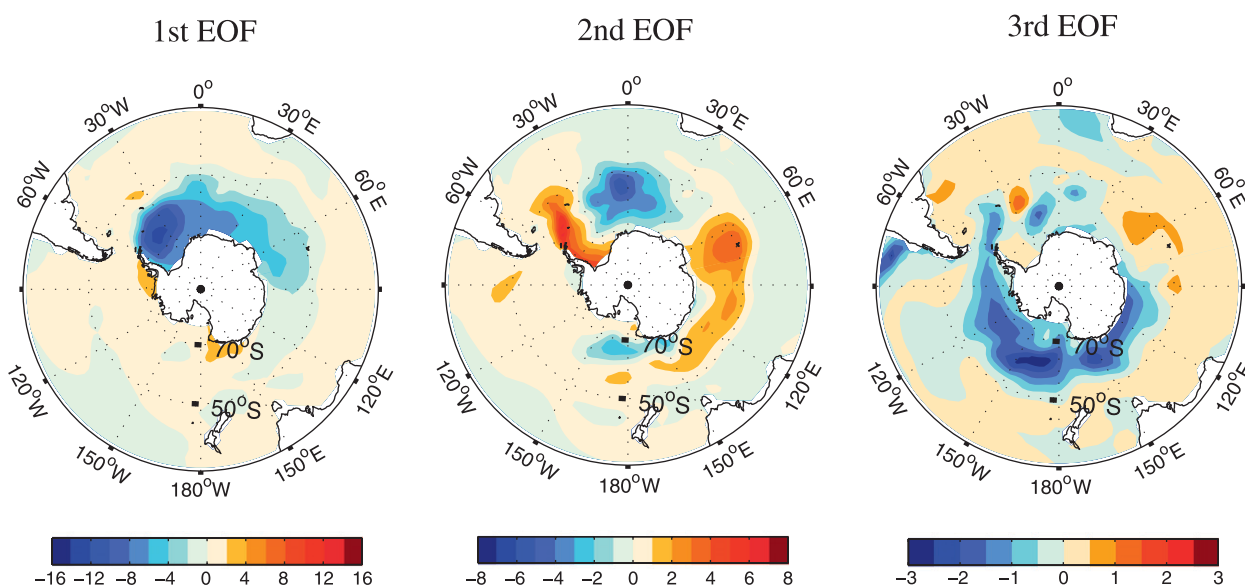


FIG. 8. First three leading EOFs of surface  $\Delta^{14}\text{C}$  variability in the southern extratropics: EOFs calculated as in Fig. 3.

Hall and Visbeck 2002; Marshall 2002). Figure 9 shows the first EOF of the monthly sea level pressure anomaly south of 20°S as obtained from the model and observations. Although the zonal structure is somewhat different than observed, the model captures the gross features of the observed leading EOF pattern with a correlation coefficient of 0.96. The positive SAM correlates well with small negative anomalies of  $\Delta^{14}\text{C}$  ( $\sim 1\text{‰}$ ) exclusively in the Pacific sector of the Southern Ocean, reflecting the third EOF. This association can be attributed to a strengthening of the westerlies during the positive phase of the SAM, inducing northward Ekman transport and bringing more  $^{14}\text{C}$ -depleted water from south of the Antarctic Circumpolar Current (ACC) to the north.

However, much larger amplitude variability occurs in the Weddell Sea when periodic convective events exhume  $^{14}\text{C}$ -depleted waters from the deep sea; similar, but weaker events occur in the Ross Sea as well as in the Indian sector of the Southern Ocean. These events arise from disruptions of the near-surface stratification. It is entirely possible that this mode of convection is an artifact of the coarse model resolution, particularly the lack of dense water production on shelves and weak downslope flows (Toggweiler et al. 2006). Nonetheless, the convective events are reminiscent of the Weddell Sea polynya that occurred between 1974 and 1976 (Carsey 1980), when vigorous convection occurred to a depth of 3000 m (Gordon et al. 2007). Given the similarity to what may be a natural mode of variability in the Weddell Sea and the large impact these events have on radiocarbon, we discuss the convective events in some detail.

Examination of the average annual-mean temperature stratification in the Weddell Sea (Fig. 10a) shows that, whereas surface temperatures are higher during surface  $^{14}\text{C}$ -depletion events, the waters at 300 m are actually slightly colder during convection, as wintertime cooling stirs cold water to depth. The high surface temperatures occur because convection brings up enough warm Upper Circumpolar Deep Water during the wintertime to maintain an ice-free polynya, facilitating more absorption of solar radiation and much warmer springtime temperatures. Since these changes result in increased stratification, they cannot by themselves explain the increase in convection. Instead, the cause is a breakdown in the salinity stratification, with convection exposing low  $\Delta^{14}\text{C}$  water at the surface when the salinity gradient between the surface and 300 m collapses (Fig. 10b).

We can use times when there is an anomalous decrease in surface radiocarbon [beyond one standard deviation (std dev)] to detect convective onset and times when there is an anomalous increase in surface radiocarbon to detect convective shutoff. As shown in Fig. 10c, five years

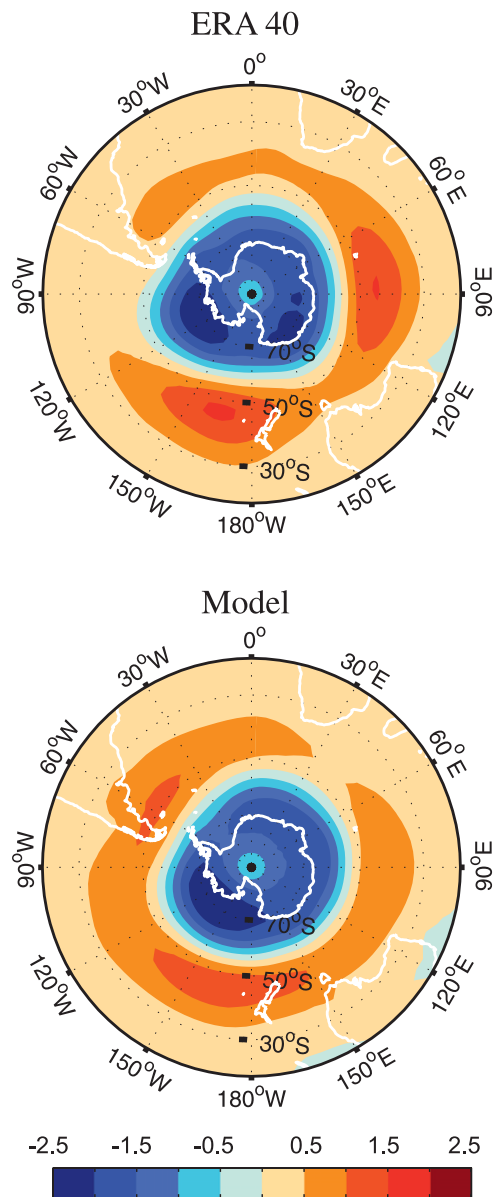


FIG. 9. Model simulation of SAM-like variability: The first EOF of the monthly sea level pressure anomaly south of 20°S is shown, as obtained from (top) observations (ERA-40) and (bottom) model, accounting for 41% and 48% of the variance, respectively.

before the onset of convection, salinities are lower than average to the west of the Antarctic Peninsula and higher to the east of 40°W. At the time of convective onset (Fig. 10d), the saline anomaly has strengthened and propagated into the central gyre. This is similar to the preconditioning mechanism for the Weddell Polynya suggested by Gordon et al. (2007), who related extended periods of a negative SAM to a buildup of salinity at the surface, destabilizing the upper water column. In the model, the simulated high-salinity anomaly reaches a

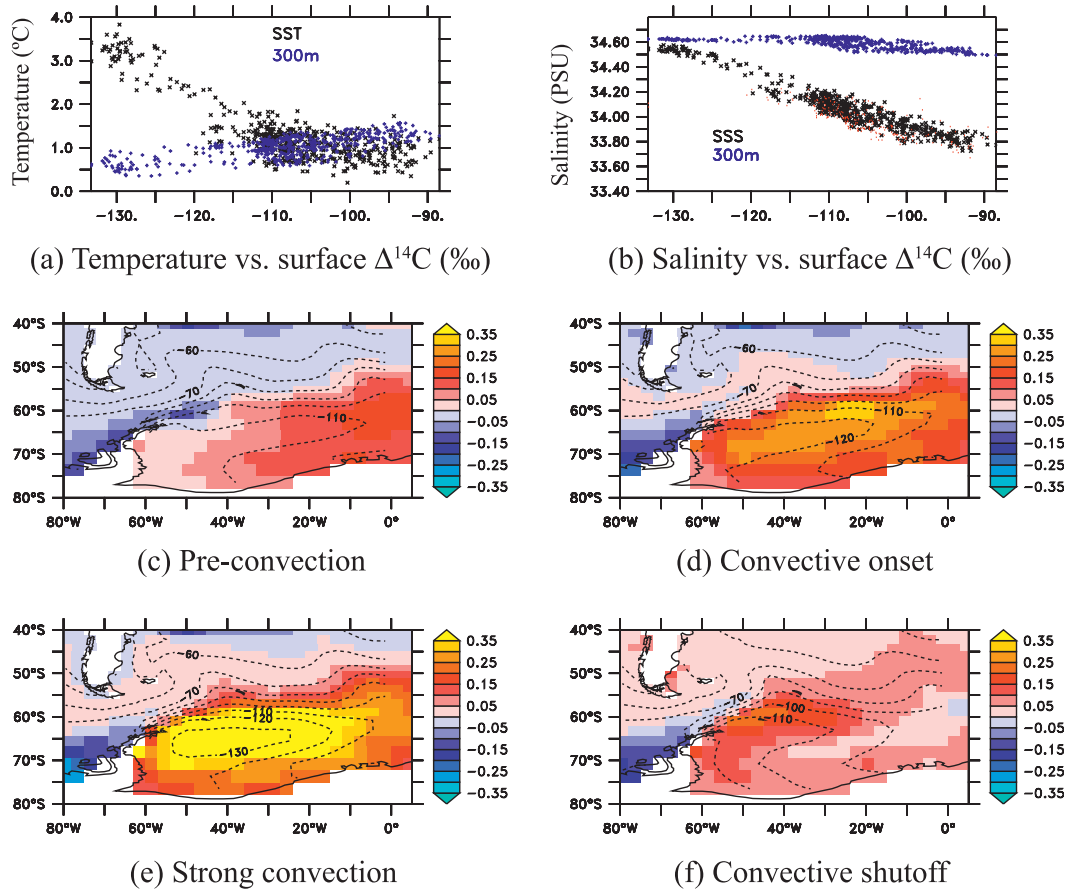


FIG. 10. Episodic convection events in the Weddell Sea: (a) water temperature at two depths vs surface  $\Delta^{14}\text{C}$ , averaged annually over  $70^{\circ}\text{--}60^{\circ}\text{S}$ ,  $50^{\circ}\text{--}30^{\circ}\text{W}$ . When convection is active, the surface  $\Delta^{14}\text{C}$  is low (left side of panel) and the surface is relatively warm but the water at 300 m is relatively cool. (b) As in (a), but showing salt instead of temperature. (c)–(f) The progression of salinity anomalies (color) in association with ventilation events, as identified by the rate of change of water age on a 300-m depth surface between  $70^{\circ}$  and  $60^{\circ}\text{S}$ ,  $50^{\circ}$  and  $30^{\circ}\text{W}$ . Dashed contours show surface  $\Delta^{14}\text{C}$ , in permil.

maximum at the height of convective activity, partly due to mixing with the saline waters below (Fig. 10e). Finally, as fresher water is advected from the east along the southern flank of the gyre, the high salinity, low  $\Delta^{14}\text{C}$  anomaly dwindles and the convection shuts off (Fig. 10f). Convective events are generally followed by a multi-decadal period of greater near-surface stability in the Weddell Sea, with higher  $\Delta^{14}\text{C}$  at the surface.

#### 4. Variability in the air–sea flux of radiocarbon

The prior section discussed redistributions of radiocarbon within the ocean due to changes in ocean mixing and advection. However, oceanic radiocarbon is also altered by changes in the air–sea balance of radiocarbon that, in turn, alter the radiocarbon activity of the relatively small atmospheric reservoir. Although we do not explicitly model atmospheric  $^{14}\text{C}$  here, we can infer its

behavior by analyzing the air–sea fluxes. Below, we illustrate how the sea surface  $\Delta^{14}\text{C}$  distribution and the wind-speed-dependent air–sea exchange both vary the air–sea flux of radiocarbon.

##### a. The disequilibrium flux

The air–sea fluxes of  $^{12}\text{C}$  and  $^{14}\text{C}$  are highly correlated in space and time, as are their anomalies (Fig. 11). This is because, despite globally lower saturation states for  $^{14}\text{C}$ , most of the spatial and temporal variability in the saturation state of both isotopes is driven by changes in water temperature and the biological pump of carbon. To highlight differences between the fluxes, which are responsible for changing the  $\Delta^{14}\text{C}$  of the atmosphere, we use the concept of a “disequilibrium  $^{14}\text{C}$  flux,” as introduced by Rodgers et al. (2011). This construct simply normalizes the air–sea flux of  $^{14}\text{C}$  relative to that of  $^{12}\text{C}$ , to avoid the unwieldy fact that their concentrations differ

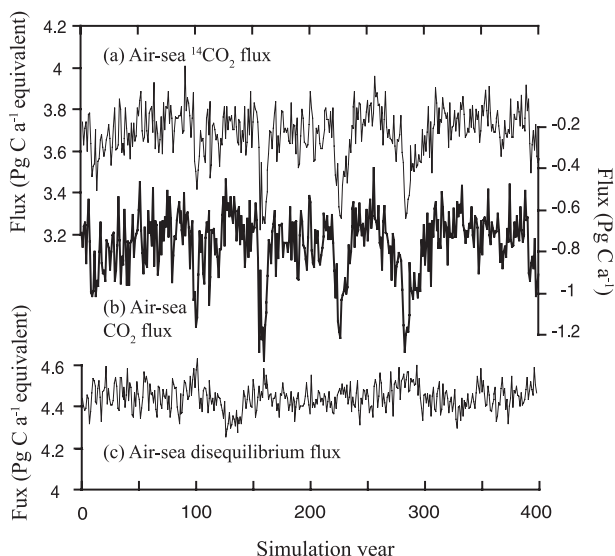


FIG. 11. Air-sea flux time series: (a) Annual global integral of  $^{14}\text{CO}_2$  across the air-sea interface, positive fluxes into the ocean. The time series was linearly detrended, and the flux is shown as  $\text{Pg C yr}^{-1}$ . As in (a), but (b) for  $\text{CO}_2$  and (c) for the disequilibrium flux, which controls the air-sea balance of radiocarbon.

by approximately 12 orders of magnitude, allowing a straightforward comparison. The disequilibrium flux is defined as

$$\phi_{\text{diseq}} = \phi_{14\text{C}} r_{1890}^{12/14} - \phi_{12\text{C}}, \quad (1)$$

where  $\phi_{12\text{C}}$  is the air-sea  $^{12}\text{C}$  flux and  $\phi_{14\text{C}}$  the air-sea  $^{14}\text{C}$  flux. The disequilibrium flux is given as  $^{12}\text{C}$ -equivalent units of  $^{14}\text{C}$  and can be integrated globally to provide the net effect of air-sea exchange on atmospheric  $\Delta^{14}\text{C}$ . According to the convention used here, a positive disequilibrium flux indicates a net transfer of  $^{14}\text{C}$  into the ocean such that the atmospheric  $\Delta^{14}\text{C}$  would decrease.

Figure 11 shows that the disequilibrium flux is a relatively invariant residual between the much more variable  $^{14}\text{C}$  and  $^{12}\text{C}$  fluxes. Moreover, the temporal structure of the disequilibrium flux is very different from that of  $^{14}\text{C}$  and  $^{12}\text{C}$ . For example, four intense multiyear anomalies, associated with the Weddell Sea convection events discussed above, show strong, highly correlated decreases in the flux of both  $^{12}\text{C}$  and  $^{14}\text{C}$  into the ocean owing to the high dissolved inorganic carbon (DIC) concentration of the exposed deep waters (Fig. 11). The high degree of correlation causes changes in the disequilibrium flux to be relatively small.

Figure 12 provides an alternate perspective, showing the interannual variability of the zonally integrated disequilibrium flux, compared to the interannual variability of surface  $\Delta^{14}\text{C}$ . The surface  $\Delta^{14}\text{C}$  variability is

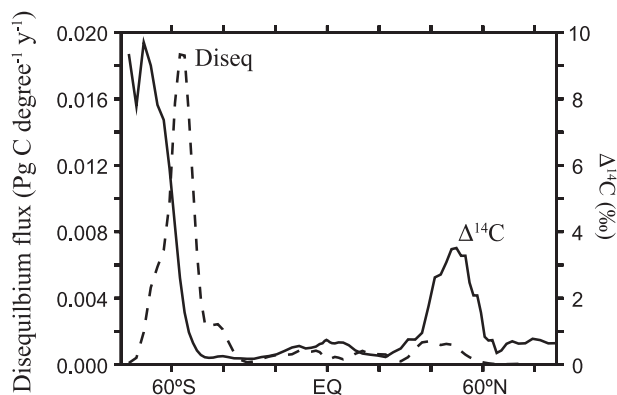


FIG. 12. Interannual variability in air-sea fluxes by latitude: interannual variability of surface  $\Delta^{14}\text{C}$  (1 std dev) zonally averaged (solid line, right ordinate) and the interannual variability of the disequilibrium flux (1 std dev) zonally integrated (dashed line, left ordinate).

large at high latitudes of the North Pacific and Southern Ocean, as expected from the analysis in section 3. However, the strongest disequilibrium flux variability is centered at  $58^\circ\text{S}$ . As discussed by Rodgers et al. (2011), this portion of the Southern Ocean also dominates the magnitude of the integrated global disequilibrium flux due to the low  $^{14}\text{C}$  content of deep waters drawn up to the south and the large area in which strong winds drive rapid air-sea exchange.

### b. Mechanisms of variability

To understand the mechanisms underlying the the air-sea balance of radiocarbon, it is instructive to recall that, in the model, the air-sea exchange flux  $\phi_{12\text{C}}$  scales with

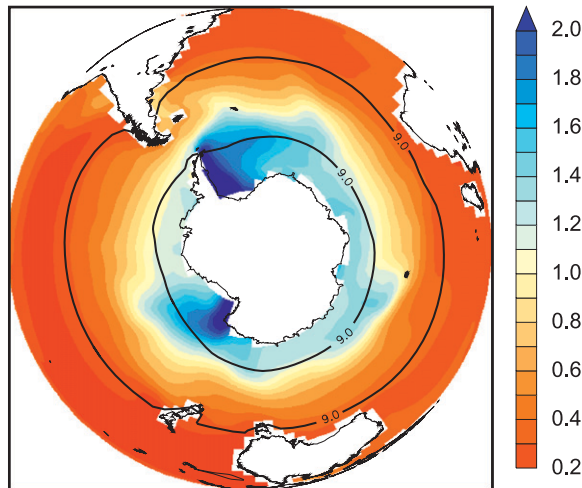
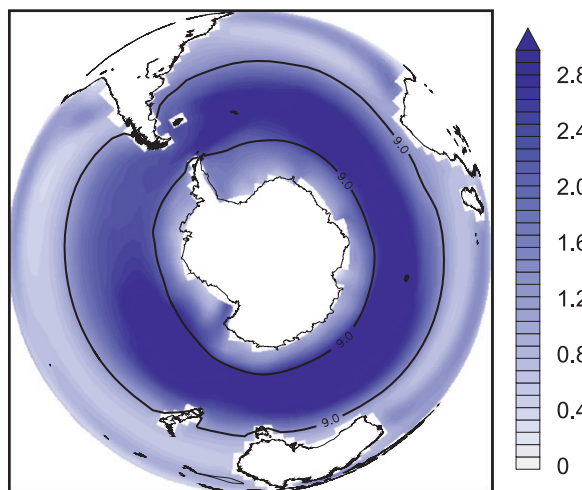
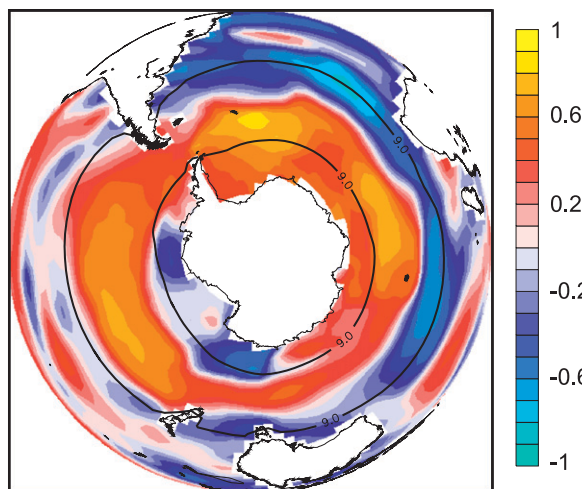
$$U_{10}^2 [C(\text{surf})_{\text{sat}} - C(\text{surf})], \quad (2)$$

where  $U_{10}$  is the wind speed at 10-m elevation,  $C(\text{surf})$  is the sum of dissolved  $\text{CO}_2$  and  $\text{H}_2\text{CO}_3$ , and  $C(\text{surf})_{\text{sat}}$  is  $C(\text{surf})$  at saturation (largely a function of temperature and salinity). Because  $^{14}\text{C}(\text{surf})_{\text{sat}}$  is equal to  $C(\text{surf})_{\text{sat}} r_a^{14/12}$ , where  $r_a^{14/12}$  is the atmospheric  $^{14}\text{C}/^{12}\text{C}$ , the air-sea flux of  $^{14}\text{CO}_2$ ,  $\phi_{14\text{C}}$ , scales with

$$U_{10}^2 [C(\text{surf})_{\text{sat}} r_a^{14/12} - ^{14}\text{C}(\text{surf})]. \quad (3)$$

In the special case where atmospheric  $\Delta^{14}\text{C}$  is  $0\text{‰}$ , that is,  $r_a^{14/12} = 1/r_{1890}^{12/14}$ , we can define  $^{14}\text{C}(\text{surf})^*$  as  $^{14}\text{C}(\text{surf}) r_{1890}^{12/14}$  (similar to our disequilibrium flux convention) so that, by substitution of Eqs. (2) and (3) in Eq. (1), the disequilibrium flux  $\phi_{\text{diseq}}$  scales with

$$U_{10}^2 [C(\text{surf}) - ^{14}\text{C}(\text{surf})^*]. \quad (4)$$

(a) Surface water  $C_{\text{surf}} - {}^{14}C_{\text{surf}}^*$  ( $\mu\text{mol kg}^{-1}$ )(b) Disequilibrium flux ( $\text{mol m}^{-2} \text{a}^{-1}$ )

(c) Correlation of local disequilibrium flux with global disequilibrium flux (40-yr smoothed)

Figure 13a shows  $[C(\text{surf}) - {}^{14}C(\text{surf})^*]$  at the surface layer of the Southern Hemisphere during May, a time of vigorous exchange. High values occur close to Antarctica owing to the mixing with waters below, north of which they decrease; this is very nearly a mirror image of the surface  $\Delta^{14}C$ . Figure 13b shows the time-averaged disequilibrium flux  $\phi_{\text{diseq}}$ . The disequilibrium flux is clearly focused within the southern portion of the westerly wind belt, indicated here as the region between the two black contour lines (time-averaged surface winds between these contours exceed  $9 \text{ m s}^{-1}$ ). The high disequilibrium flux per unit area within this belt is due to the coincidence of large  $[C(\text{surf}) - {}^{14}C(\text{surf})^*]$  and strong winds. In addition to the weaker winds, air-sea exchange at higher latitudes is impeded by winter sea ice (not shown).

The final panel of Fig. 13 shows the correlation coefficient ( $r$ ) between the local disequilibrium flux and the global disequilibrium flux (both smoothed with a 40-yr boxcar filter). The relatively high correlation within the westerly wind belt is due to the strong role that this zone plays in controlling the global air-sea balance of radiocarbon. Notably, the local disequilibrium flux north of  $\sim 45^\circ\text{S}$  is often anticorrelated with the global disequilibrium flux owing to the fact that winds in this region tend to be weaker when winds intensify within the westerly belt, that is, during positive phases of the SAM; however, this more northerly region has little impact on the global integral because of the small magnitude of the disequilibrium flux there (Fig. 13b). Instead, the southern part of the wind belt dominates the air-sea balance variability.

The control by the winds is locally very important on short time scales, with very strong local correlation ( $r > 0.9$ ) at most points in the ocean, because of the quadratic dependence of the disequilibrium flux on wind speed (Wanninkhof 1992) and the fact that  $(C(\text{surf}) - {}^{14}C(\text{surf})^*)$  is positive everywhere in the surface ocean. However, on longer time scales, the globally integrated

←

FIG. 13. Radiocarbon exchange in the Southern Ocean. (a) The concentration of  $C(\text{surf}) - {}^{14}C(\text{surf})^*$  at the sea surface. The air-sea disequilibrium flux is determined by the product of this difference and the square of the wind speed. The band of the Southern Ocean with annually averaged windspeeds in excess of  $9 \text{ m s}^{-1}$  lies between the two black contours. (b) The mean disequilibrium flux. (c) Correlation between annual integrals of the local disequilibrium flux and the global disequilibrium flux, with a 40-yr boxcar smoothing. Positive correlations indicate where local changes in the disequilibrium flux tend to covary with the global disequilibrium flux.

flux is dominated by the air–sea gradient. This dominance is illustrated by the temporal correlation of the global disequilibrium flux and the average  $\Delta^{14}\text{C}$  of the global surface ocean on long time scales ( $r = -0.87$ , boxcar 20 yr smooth, rather than  $r = -0.54$  for interannual variations). Because the westerlies drive the upwelling of  $^{14}\text{C}$ -depleted waters to the Southern Ocean surface, in addition to their role in accelerating local air–sea exchange within the wind belt, they play a central part in setting the air–sea balance of radiocarbon (Rodgers et al. 2011); however, the high frequency of the model SAM limits its ability to drive decadal–centennial changes in upwelling in the simulations shown here.

### c. Simulated changes in atmospheric radiocarbon

Despite the demonstrated potential for the Southern Ocean to drive changes in the air–sea balance of  $^{14}\text{C}$ , the variability exhibited by the simulation shown here would have little impact on the resultant atmospheric  $\Delta^{14}\text{C}$ . We estimate the expected atmospheric response by removing the detrended average flux of  $\phi_{\text{diseq}}$  into the ocean, which balances the decay of radiocarbon within the global ocean and model drift, to estimate the effect of variable air–sea exchange on the atmospheric  $^{14}\text{C}$  and  $^{12}\text{C}$  inventories. Starting from  $0\text{‰}$ , we integrate the air–sea fluxes, assuming an atmospheric C inventory of 600 Pg, a terrestrial biosphere of 2200 Pg, and an exchange between them of  $60 \text{ Pg yr}^{-1}$  (Hughen et al. 2004). Note that this calculation will overestimate true changes in atmospheric  $\Delta^{14}\text{C}$  since, over time, an increase (decrease) in atmospheric  $\Delta^{14}\text{C}$  will drive an increased (decreased) disequilibrium flux back into the ocean, ignored by our use of a constant atmospheric  $\Delta^{14}\text{C}$  of  $0\text{‰}$ . Figure 14 shows the prediction of atmospheric  $\Delta^{14}\text{C}$  variability that results from this calculation over the last 400 yr of unforced variability in the model. Comparison to Fig. 1 clearly shows that the magnitude of atmospheric  $\Delta^{14}\text{C}$  variability estimated from model  $\phi_{\text{diseq}}$  is much smaller than that reconstructed from tree-ring records of atmospheric  $\Delta^{14}\text{C}$ : less than  $\pm 1\text{‰}$ , an order of magnitude smaller than the reconstructed changes.

Two possible, nonexclusive conclusions could be drawn from the small amplitude of the simulated variability. The first possibility is that, despite the apparent fidelity of the simulated modes of interannual variability, unforced variability in the model is significantly smaller than that of the real world on multidecadal time scales. Indeed, the lack of variability in the radiative boundary conditions, such as fluctuations in solar input, volcanic activity, and stratospheric chemistry, could be expected to produce an insufficiently variable simulation. In particular, if southern westerlies and/or stratification of the polar haloclines have undergone significant low-frequency variability,

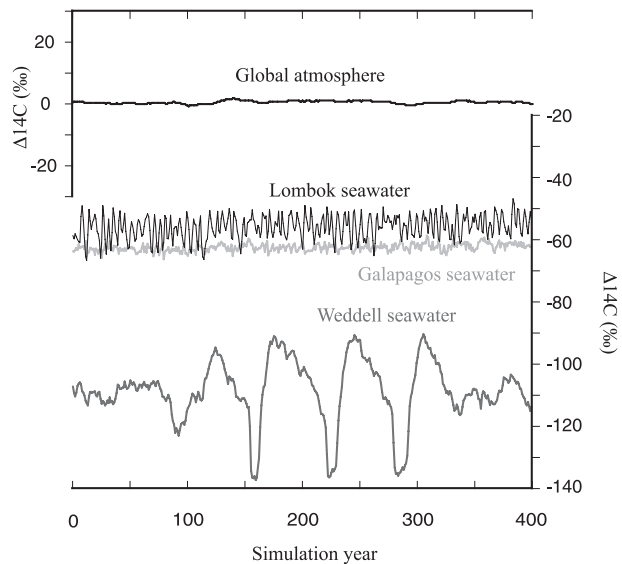


FIG. 14. Simulated atmospheric and seawater  $\Delta^{14}\text{C}$  arising from unforced model variability over 400 yr: the upper curve approximates the variations in global atmospheric  $\Delta^{14}\text{C}$  expected from the simulated air–sea disequilibrium flux, as described in the text. The lower curves show the simulated variations in sea surface  $\Delta^{14}\text{C}$  in the model (Galapagos seawater, eastern Indian Ocean near Lombok Strait, and the central Weddell seawater). The axes are scaled to be approximately equivalent to the corresponding data shown in Fig. 1.

it could have resulted in larger disequilibrium flux variability than simulated here. This may be testable against observations in future, given well-constrained  $^{14}\text{C}$  production rates and through comparison to the interhemispheric gradient of atmospheric  $\Delta^{14}\text{C}$  derived from tree rings (Rodgers et al. 2011).

The second possibility is that natural, decadal to centennial time-scale changes in air–sea exchange had little impact on atmospheric  $\Delta^{14}\text{C}$  during the preindustrial, postdeglacial period. This possibility would require the production rate of  $^{14}\text{C}$  by cosmic rays to have been the primary driver of observed atmospheric  $\Delta^{14}\text{C}$  variability during the Holocene. Indeed, this argument was put forth by previous workers based on scaling arguments, including Stuiver and Quay (1980) and Siegenthaler et al. (1980). In addition, a production-rate control on atmospheric  $^{14}\text{C}$  is supported by radionuclide production records derived from  $^{10}\text{Be}$  abundances in ice cores (Bard et al. 2000; Muscheler et al. 2007) and is commonly assumed by those interpreting the atmospheric radiocarbon record as an indicator of solar output over the Holocene (Knudsen et al. 2009). If true—that is, if the simulated disequilibrium flux variability is not dramatically less than the true variability—this would simplify the interpretation of both atmospheric and oceanic records of  $\Delta^{14}\text{C}$  over the Holocene.

## 5. Conclusions

The CM2Mc model simulation explored here exhibits modes of interannual variability similar to ENSO, the AO, and the SAM, as characterized by observations. Overall, the CM2Mc tropical and ENSO biases are qualitatively similar in character to those seen in the higher-resolution model, CM2.1 (Wittenberg 2009), though somewhat larger in amplitude. This suggests that CM2Mc may provide a cost-effective new tool to explore the causes of these biases, which are shared among many state-of-the-art CGCMs (Guilyardi et al. 2009) and complicate future projections of tropical climate and ENSO (Collins et al. 2010; Vecchi and Wittenberg 2010). In addition, the model is well suited for long (millennial time scale) simulations.

The distribution of radiocarbon within the model was well correlated with these modes of interannual variability, with distinct relationships linking tropical  $^{14}\text{C}$  to Niño-3 SST, as previously shown with forced ocean models (Rodgers et al. 1997). The modeled surface water  $\Delta^{14}\text{C}$  at the Galapagos site (Fig. 14) is remarkably stable in contrast to the observed variability (Fig. 1). This disagreement suggests that the unforced model underestimates true variability at this site, perhaps due to difficulties in capturing the fine details of the equatorial current structure of Galapagos and/or resolving tropical instability waves, possibilities that we leave to further investigation. In contrast, in the vicinity of the Indonesian Throughflow, the modeled variability (1 std dev = 3.8‰) is of similar magnitude to that observed in corals (1 std dev = 4.2‰, Guilderson et al. 2009). Although there are certainly problems with the model's ability to resolve the complex Indonesian Throughflow region as well, it does support this location as a particularly sensitive location in which to use coral  $\Delta^{14}\text{C}$  as a monitor of circulation changes (Fig. 14) owing to the coincidence of strong  $\Delta^{14}\text{C}$  gradients with variable water transport.

Meanwhile, the variability of  $^{14}\text{C}$  at the surface of the Southern Ocean was dominated by changes in deep convection on a multidecadal time scale. In the model, these convection events are not obviously related to the relatively high frequency SAM but are associated with dramatic changes in sea surface salinity. In the Weddell Sea, salty anomalies originate near the prime meridian due to atmospheric forcing and advect southwestward toward the gyre center where they set off vigorous convection. The convection brings warm,  $^{14}\text{C}$ -depleted, deep water to the surface until the halocline reestablishes itself (Fig. 14). Given the difficulty of representing convection accurately in a global, level-coordinate ocean model, the details of this mechanism must be regarded with some caution. Indeed, they are reminiscent of "flushing" events,

noted in coarse-resolution models with mixed boundary conditions (Winton and Sarachik 1993) and may reflect the inability of the model to produce dense waters on shelves, as occurs in nature (Toggweiler et al. 2006). Nonetheless, the Weddell Polynya of 1974–76 appears to have been very similar to our simulated convective events (Gordon et al. 2007), suggesting that this is a real mode of variability, even if perhaps exaggerated by the model. If so, radiocarbon records may help to document the occurrence of Weddell Sea polynyas that predated the satellite era (e.g., Domack et al. 2001).

Although the simulated variability of  $\Delta^{14}\text{C}$  in the Weddell Sea was dramatic, the resulting local disequilibrium flux anomalies did not dominate the global integral, given their restricted areal extent. Instead, the global air–sea disequilibrium flux was dominated by exchange within the westerly wind belt over the open Southern Ocean. There, high wind speeds and ice-free winters conspire with the low  $\Delta^{14}\text{C}$  of upwelling Upper Circumpolar Deep Water to drive most of the global disequilibrium flux, as discussed by Rodgers et al. (2011). When the  $\Delta^{14}\text{C}$  of waters exposed in this region of vigorous air–sea exchange decreased, an increased disequilibrium flux of  $^{14}\text{C}$  into the ocean tended to occur.

Nonetheless, the magnitude of simulated air–sea disequilibrium anomalies was insufficient to alter atmospheric  $\Delta^{14}\text{C}$  by more than a few permil (Fig. 14), far less than the magnitude of the Suess wiggles (~20‰, Fig. 1). This discrepancy may indicate that natural variability in the climate system, produced by external forcings or internal feedbacks, significantly exceeds that of the model. In particular, large changes in the position or strength of the Southern Hemisphere westerlies may have caused sustained changes in the disequilibrium flux not captured here (Rodgers et al. 2011). However, previous authors have presented evidence that the Suess wiggles were dominated by changes in the production rate of  $^{14}\text{C}$ , caused by fluctuations in the geomagnetic field and solar activity (Stuiver and Quay 1980; Bard et al. 2000; Muscheler et al. 2007), and the results here do not provide any reason to disagree with this interpretation.

This paper has used an earth system model simulation to explore  $\Delta^{14}\text{C}$  variability at the sea surface on decadal to centennial time scales, given steady boundary conditions and constant atmospheric  $\Delta^{14}\text{C}$ , and linked this variability to modeled climate modes. Future modeling work could explore the effect of changes in radiative (or other) boundary conditions and how variability in the production rate of  $^{14}\text{C}$  propagates through the system. The development of new high-resolution radiocarbon records in regions with significant  $\Delta^{14}\text{C}$  variability could help to constrain climate

modes on long time scales, identify model biases, and contribute to developing improved understanding of natural climate variability.

*Acknowledgments.* We thank Ellen Druffel for providing coral data and for comments on an early draft of the manuscript, and Michael Winton, Matthew Harrison, and Hyo-Seok Park for discussions. Sergey Malyshev assisted with the land model. Robbie Toggweiler and Stephanie Downes provided internal reviews. Karen Assmann and two anonymous reviewers provided thoughtful, constructive comments. The OAA\_OI\_SST\_V2 data was provided by the NOAA/OAR/ESRL PSD, Boulder, Colorado, from their Web site at <http://www.esrl.noaa.gov/psd/> and ECMWF ERA-40 data were provided by ECMWF and have been obtained from the ECMWF Data Server. This work was supported by the Natural Sciences and Engineering Research Council of Canada (NSERC), the Canadian Institute for Advanced Research (CIFAR), and the Carbon Mitigation Initiative (CMI) project at Princeton University, sponsored by BP and Ford Motor Company. This paper was prepared by Eric Galbraith under awards NA17RJ2612 and NA08OAR4320752 from the National Oceanic and Atmospheric Administration (NOAA), U.S. Department of Commerce. The statements, findings, conclusions, and recommendations are those of the authors and do not necessarily reflect the views of the National Oceanic and Atmospheric Administration or the U.S. Department of Commerce.

## APPENDIX A

### Model Description

This paper presents the Coupled Model 2 with Modular Ocean Model version 4p1 (MOM4p1) at coarse resolution (CM2Mc). This model is similar to the Geophysical Fluid Dynamics Laboratory (GFDL) 1° coupled model (CM2.1) (Delworth et al. 2006), used in the Intergovernmental Panel on Climate Change Fourth Assessment Report. However, the resolution of both atmospheric and oceanic grids has been coarsened so as to decrease computational cost, and the model uses an updated version of the GFDL code, prepared in anticipation of a suite of simulations for the IPCC Fifth Assessment Report. This updated code includes the ocean model MOM4p1 (Griffies 2009), which includes a number of numerical and physical improvements, as well as the option of using pressure for the vertical coordinate instead of depth so that steric sea level is directly simulated. Modifications made to the CM2.1 atmosphere are minor, involving a reduction of spatial resolution and

minimal parameter changes. More substantial changes were made to the ocean component, including improvements to the subgrid-scale parameterizations of ocean mixing, which is of critical importance to low-resolution climate models incapable of explicitly representing processes such as mesoscale eddies and gravity-driven bottom flows. CM2Mc requires approximately one tenth the computational cost of the higher resolution model CM2M. Additional model configuration details and diagnostics can be found on the Web site <http://sites.google.com/site/cm2cmodel/>.

#### *a. Atmospheric model configuration*

The atmosphere is very similar to the GFDL Atmospheric Model 2 (AM2), as described by the GFDL Global Atmospheric Model Development Team (Anderson et al. 2004), but using the finite volume dynamical core of Lin (2004), as implemented in CM2.1 (Delworth et al. 2006). The atmosphere used here employs the M30 grid, with a latitudinal resolution of 3° and a longitudinal resolution of 3.75°, instead of the M45 grid used in CM2.1 (2° by 2.5°), but uses the same vertical configuration with 24 levels. The decreased horizontal resolution results in 44% of the number of grid cells in the CM2.1 atmosphere, a relatively modest decrease in resolution. However, the atmospheric time steps are also increased, from 0.5 to 1.5 h for the tracer time step, from 6 to 9 min for the dynamical time step, and from 2 to 3 h for the radiative time step. The coupled model includes an explicit representation of the diurnal cycle of solar radiation.

The change in discretization required a small readjustment of two cloud parameters (the critical droplet threshold radius and the cloud erosion time scale) to maintain a net radiation balance close to zero under modern climate, which had negligible impact on atmospheric dynamics. In addition, the mountain gravity drag parameter  $G^*$  (Anderson et al. 2004) was decreased from 1.0 to 0.5 to compensate for the coarser horizontal resolution. The final alteration was the replacement of the sea salt aerosol climatology of Haywood et al. (1999), used for the radiative conditions, with a more recent estimate from Ginoux et al. (2006). As in CM2.1, the Land Dynamics model of Milly and Shmakin (2002) is used, including a river routing scheme but no terrestrial ecosystem (see Anderson et al. 2004).

#### *b. Ocean grid and bathymetry*

The CM2Mc ocean uses a tripolar grid (Murray 1996) to avoid the grid singularity at the north pole, as in the GFDL CM2.0 and CM2.1 models (Griffies et al. 2005; Gnanadesikan et al. 2006). The horizontal dimensions of the ocean grid vary according to latitude, with the finest latitudinal resolution of 0.6° at the equator allowing

TABLE A1. Parameter values used in the iBGC biogeochemical model.

Variable	Description	Value	Unit
$k$	Temperature dependence of growth	0.0378	$^{\circ}\text{C}^{-1}$
$k_r$	Temperature dependence of remineralization	0.0249	$^{\circ}\text{C}^{-1}$
$v_{\text{max}}$	Maximum $\text{PO}_4$ uptake rate at $0^{\circ}\text{C}$	0.0216	$\mu\text{mol kg}^{-1} \text{day}^{-1}$
$k_{\text{PO}_4}$	$\text{PO}_4$ uptake half-saturation constant	0.1	$\mu\text{mol kg}^{-1}$
$\text{irr}_k$	Light half-saturation constant	20	$\text{W m}^{-2}$
$\phi_{\text{DOP}}$	Fraction of nonparticulate uptake to DOM	0.65	Unitless
$\gamma_{\text{DOP}}$	Decay time scale of DOM	2.56	$\text{yr}^{-1}$
C:P	Carbon to Phosphorus ratio in organic matter	106	$\text{mol C mol P}^{-1}$
$w_{\text{sink}_0}$	Initial sinking rate	12	$\text{m day}^{-1}$
$w_{\text{sink}_{\text{acc}}}$	Acceleration rate of sinking with depth	0.09	$\text{day}^{-1}$
$\gamma_{\text{POP}}$	Remineralization rate of sinking POM	0.04	$\text{day}^{-1}$

an explicit physical representation of some equatorial currents. There are 28 vertical levels, the uppermost eight of which are each 10 dbar thick below which the levels gradually increase in thickness to a maximum of 506 dbar. The model employs partial bottom cells (Adcroft et al. 1997; Pacanowski and Gnanadesikan 1998) to allow a more realistic representation of the bathymetry.

The bathymetry was initially generated from averaging satellite-derived bathymetry onto the coarser model grid with a smoothing algorithm. The result was then carefully examined, and critical features destroyed in the regridding process were manually restored. To compensate for mixing between ocean basins and marginal seas where the coarse resolution of the topography does not resolve the narrow connections, the cross-land mixing scheme of Griffies et al. (2005) is employed, generating less than 2 Sv of total mixing at each of six locations. Finally, where the discharge locations for precipitation falling on Antarctica led to the margins of the Ross or Filchner–Rønne Ice Shelves, they were shifted north of the coast by a few degrees, so as to roughly account for the transport of freshwater by drifting icebergs.

### c. Ocean–ice model and parameterizations

CM2Mc uses the MOM4p1 code with pressure as the vertical coordinate, thus allowing the model to solve the non-Boussinesq primitive equations. This is coupled to the GFDL thermodynamic–dynamic sea ice model (SIS) (Delworth et al. 2006). The vertically integrated mode is time stepped using an explicit bottom pressure solver, and the transfer of water mass across the ocean surface occurs using real freshwater fluxes. Tracer advection uses the Multidimensional Piecewise Parabolic Method (MDPPM) scheme for temperature and salinity (Adcroft et al. 2004), and the Sweby Multidimensional Flux Limited (MDFL) scheme for other tracers (Griffies et al. 2005). Light is absorbed by water and a chlorophyll field following the Manizza et al. (2005) algorithm. Over

the initial millennium of simulation a smoothly varying, satellite-derived climatological chlorophyll field was used, after which the chlorophyll concentrations used for shortwave absorption were those predicted by a coupled biogeochemical model [Biogeochemistry with Light, Iron, Nutrients and Gases (BLING), described by Galbraith et al. (2010), not shown here]. The gross metrics of the simulation did not change significantly with the change to prognostic chlorophyll.

Most subgrid-scale parameterizations for mixing are similar to those used in the CM2 series (Griffies et al. 2005). The lateral friction uses an isotropic Smagorinsky viscosity in midlatitudes, while within  $20^{\circ}$  of the equator the anisotropic National Center for Atmospheric Research viscosity is used (Large et al. 2001; Smith and McWilliams 2003). Lateral diffusion and skew diffusion of tracers along isopycnals is represented using the parameterization of Gent and McWilliams (1990) with a spatially varying diffusion coefficient,  $A_{\text{GM}}$ , as determined in CM2.1 (Griffies et al. 2005). The coefficient depends on the horizontal shear between 100 and 2000 m. A minimum coefficient of  $200 \text{ m}^2 \text{ s}^{-1}$  and a maximum coefficient of  $1400 \text{ m}^2 \text{ s}^{-1}$  are imposed. The slope-dependent thickness transport also stops increasing at a value of  $A_{\text{GM}}S_{\text{max}}$ , where the maximum isopycnal slope  $S_{\text{max}}$  is set to 0.01, whereas it is set to 0.002 in CM2.1 (see Gnanadesikan et al. 2007 and Farnetti et al. 2010 for discussions of this parameter). Overall, these changes generate a more active eddy mixing parameterization than CM2.1, with a greater responsiveness to changes in baroclinicity, as suggested by recent observations in the Southern Ocean (Böning et al. 2008). Meanwhile, the neutral diffusion coefficient for tracers,  $A_T$ , is set to a constant value of  $800 \text{ m}^2 \text{ s}^{-1}$ .

Within the boundary layer, we use the  $K$ -profile parameterization of Large et al. (1994). Away from the boundary layer, a background diffusivity of  $0.1 \times 10^{-4} \text{ m}^2 \text{ s}^{-1}$  and a background viscosity of  $1 \times 10^{-4} \text{ m}^2 \text{ s}^{-1}$  are used. Below 300 m, these background coefficients are punctuated by locally intense vertical mixing, as shown by tracer studies

(Naveira Garabato et al. 2004). This local mixing occurs as part of the  $K$ -profile parameterization, where convection is driven by along-isopycnal mixing and where the shear is large relative to the stratification, as well as where gravity waves are generated over regions of rough topography and break as they propagate upward into the water column. The latter process is parameterized with the tidally dependent mixing scheme of Simmons et al. (2004), which depends on local stratification as well as prescribed bottom roughness and tidal amplitude. In addition, tidal mixing in coastal areas is simulated by the mixing scheme of Lee et al. (2006).

#### d. Marine biogeochemical model

We use a new idealized ocean biogeochemistry (iBGC) model to simulate radiocarbon distributions, based on simple representations of nutrient uptake and remineralization. The effect of organic matter cycling on the radiocarbon distribution is small, but we describe the model briefly here for completeness.

Conceptually, this model is very similar to the pioneering biogeochemical model of Bacastow and Maier-Reimer (1990). In brief, it carries a single prognostic inorganic macronutrient tracer, which we call phosphate ( $\text{PO}_4$ ), and represents the net activity of phytoplankton through an uptake function in all ocean grid cells as a function of temperature  $T$  and available light  $I$ . Once taken up, the macronutrient is instantaneously partitioned between

a dissolved organic phosphorus (DOP) tracer and a flux of sinking particulate organic phosphorus (POP), according to a fixed fraction  $\phi$ . The sinking of POP is not achieved by using a prognostic tracer but, instead, by instantaneously redistributing remineralized  $\text{PO}_4$  throughout the water column beneath the layer in which uptake occurred, similar to the OCMIP2 scheme (Najjar and Orr 1998). Meanwhile, DOP decays to  $\text{PO}_4$  according to a temperature-dependent first-order rate,  $\gamma = \gamma_0 e^{k_r T}$ , where  $k_r$  gives the temperature dependency of remineralization and  $T$  is temperature ( $^{\circ}\text{C}$ ). The total mass of phosphorus ( $\text{PO}_4 + \text{DOP}$ ) is conserved within the ocean. The overall equation for  $\text{PO}_4$  is

$$\frac{d\text{PO}_4}{dt} = \text{circ}(\text{PO}_4) - V_{\max} e^{kT} (1 - e^{-I/I_k}) \times \frac{\text{PO}_4}{k\text{PO}_4 + \text{PO}_4} + \gamma \text{DOP} + \text{remi}_{\text{POP}}, \quad (\text{A1})$$

where circ indicates the net effect of ocean advection and mixing,  $V_{\max}$  is the maximum uptake rate,  $k$  is a constant determining the temperature sensitivity of uptake,  $I_k$  is a constant determining the tendency for light limitation,  $\text{remi}_{\text{POP}}$  is the remineralization source of phosphorus from sinking POP, and  $k\text{PO}_4$  is a constant determining the tendency for nutrient limitation.

All parameters used in iBGC are given in Table A1.

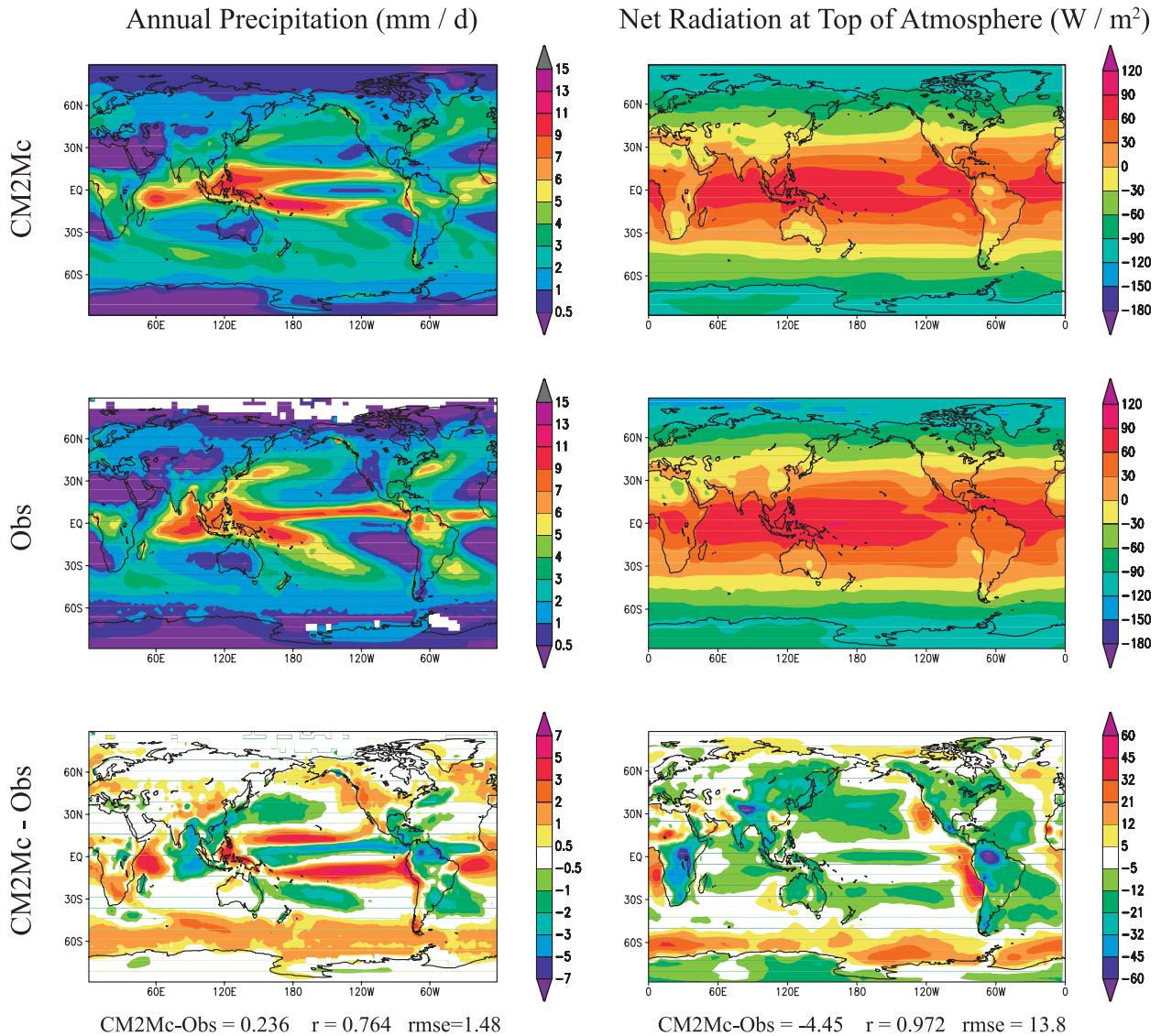


FIG. B1. Atmospheric simulation of CM2Mc: (left) annual precipitation ( $mm \text{ day}^{-1}$ ) and (right) net radiative balance across the top of the atmosphere ( $W \text{ m}^{-2}$ ), from CM2Mc and observation-based estimates. (top) Model simulation, (middle) observations of precipitation (CMAPv2 + rain gauge estimates) and radiative balance (ERBE), and (bottom) the difference between model and observations.

## APPENDIX B

### Model Simulation

#### a. Atmosphere-only simulation

As a preliminary test, the atmospheric model was integrated for twenty years with prescribed SST and constant “1990” radiative conditions, following the Atmospheric Model Intercomparison Project method described by Anderson et al. (2004). In general, this simulation shows

a very similar pattern of biases to the 2° configuration of the atmosphere, with slightly greater errors for all variables, and a radiative balance of  $+0.45 \text{ W m}^{-2}$ . The atmosphere was also tested with preindustrial radiative conditions and modern SST, in which case the radiative balance was  $-1.67 \text{ W m}^{-2}$ .

#### b. Coupled simulation

When coupled to the ocean model, the atmospheric simulation exhibits some pronounced differences in

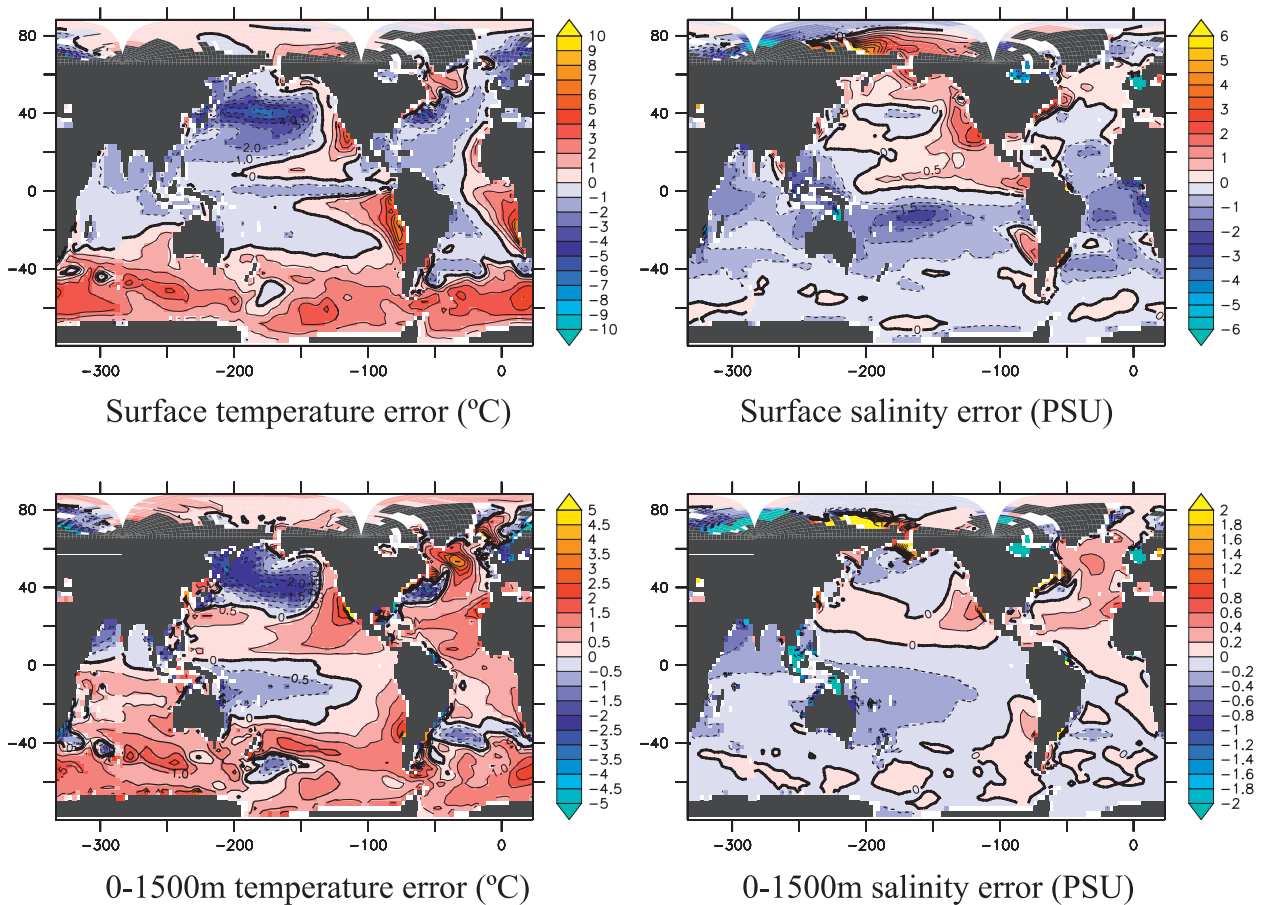


FIG. B2. Annual-mean (left) temperature and (right) salinity errors of CM2Mc (top) Sea surface compared to observations (Antonov et al. 2006; Locarnini et al. 2006) and (bottom) average errors over the upper 1500 m of the water column.

comparison to the prescribed-SST run, generally consistent with the effect of coupling the 2° M45 atmosphere to the 1° ocean of CM2.1 (Delworth et al. 2006; Wittenberg et al. 2006). Key differences include the appearance of a “split” intertropical convergence zone, that is, excessive rainfall in the Pacific just south of the equator (Fig. B1),

and an increase in the excess heating above eastern boundary upwelling regions and the Southern Ocean (Fig. B1).

When forced with preindustrial radiative conditions, the global energy balance of the coupled model is significantly more positive than in the prescribed-SST case.

TABLE B1. Ocean model metrics.

Ocean metric	CM2.1	CM2Mc	Obs	Reference
RMSE $T$ at 5 m	1.4	1.8	—	Locarnini et al. (2006)
RMSE $T$ < 1500 m	1.3	1.5	—	Locarnini et al. (2006)
RMSE $S$ at 5 m	0.82	0.97	—	Antonov et al. (2006)
RMSE $S$ < 1500 m	0.29	0.34	—	Antonov et al. (2006)
ACC (Sv)	125	156	135	Cunningham et al. (2003)
NADW at 40°N (Sv)	25	22	$20 \pm 2$	Smethie et al. (2007)
Indonesian Throughflow (Sv)	13	13.5	$12 \pm 3$	Gordon et al. (2008)
Bering Throughflow (Sv)	0.8	0.9	0.8	Woodgate and Aagaard (2005)
$\Delta^{14}\text{C}$ of NADW	—	-79	$-88 \pm 13$	Key et al. (2004)
$\Delta^{14}\text{C}$ of NPDW	—	-202	$-219 \pm 33$	Key et al. (2004)
$\Delta^{14}\text{C}$ of CDW	—	-140	$-148 \pm 22$	Key et al. (2004)

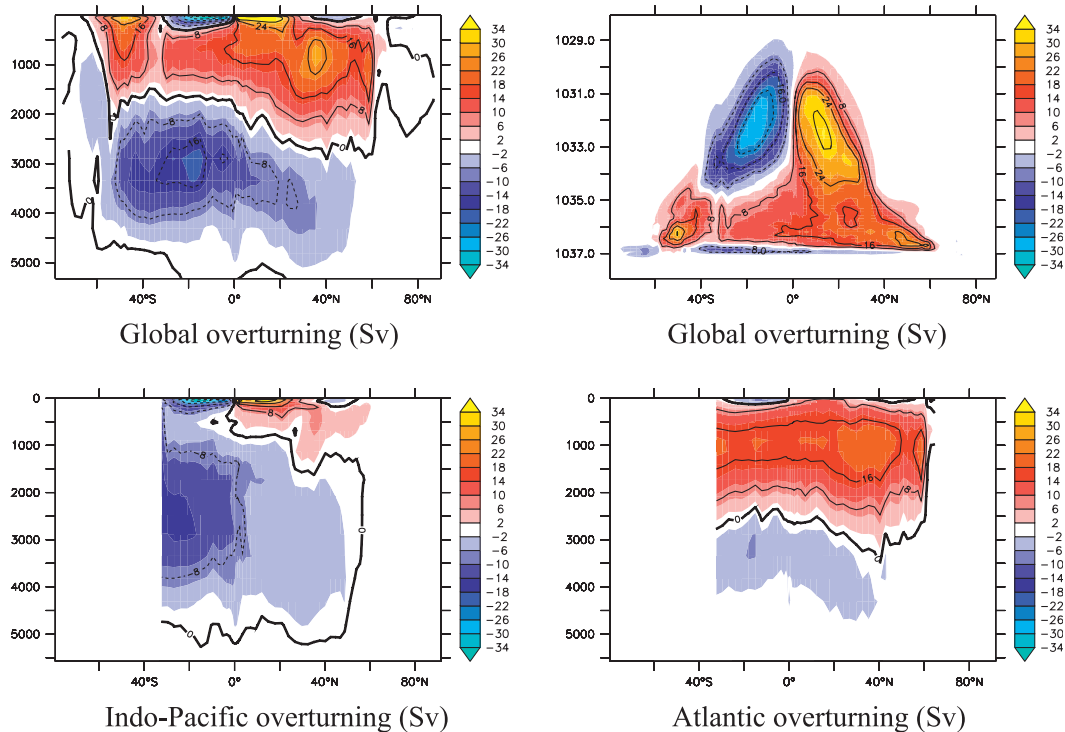


FIG. B3. Meridional overturning circulation (Sv) of CM2Mc: global overturning streamfunction as a function of (left) depth and (right) density. (bottom) Overturning streamfunction for (left) the IndoPacific and (right) the Atlantic.

The net radiation imbalance quickly rises as the ocean surface adjusts, stabilizing at  $+0.68 \text{ W m}^{-2}$  over the latter half of the first century, then gradually declines as the deep ocean warms, reaching  $\sim 0.4 \text{ W m}^{-2}$  by the end of the simulation (approximately 2000 years). Note that the atmospheric model does not conserve energy perfectly, consistently leaking  $\sim 0.4 \text{ W m}^{-2}$  owing to the fact that, unlike the ocean and land models, the atmosphere does not account for the heat content of water (Delworth et al. 2006). A time series of ocean temperature shows that the model is very close to thermal balance at the end of the simulation (not shown).

The most significant temperature and salinity errors of the ocean simulation (Fig. B2) can be attributed to the errors of the atmospheric simulation. Foremost among these are 1) a cold bias in the North Pacific, particularly during boreal summer; 2) a warm bias in the Southern Ocean, particularly during austral summer; 3) warm biases in all eastern boundary upwelling regions; and 4) a low salinity bias in the South Pacific and high salinity bias in the North Pacific (cf. Figs. B1 and B2). The first, second, and third errors can be attributed to the regional energy balances, apparently due to

inaccuracies in the representation of clouds that produce very similar errors in absorbed shortwave radiation in both the prescribed SST and coupled simulations. Meanwhile, the fourth, a result of the split ITCZ, arises from the coupling between the ocean and atmosphere in the tropical Pacific, and is a common symptom of coupled models (de Szoeke and Xie 2008). The warm bias of the Southern Ocean, combined with a tendency for North Atlantic Deep Water (NADW) to originate as excessively warm and salty, leads to a globally warm bias of the whole ocean temperature,  $4.6^\circ\text{C}$  (versus  $4.3^\circ\text{C}$  for CM2.1 and  $3.0^\circ\text{C}$  for observations, Conkright et al. 2002). Gross metrics of the ocean simulation are given in Table B1.

Compared to CM2.1, the overturning circulation is significantly different, most importantly in the circulation of deep waters formed in the Southern Ocean. CM2.1 ventilates a continuous water column throughout the Weddell Sea, evident in the ideal age and salinity sections (see Fig. 7 of Gnanadesikan et al. (2006)) and in disagreement with observations. In contrast, CM2Mc ventilates at a lower rate, closer to the Antarctic continent, evident in the overturning cell at  $\sigma_2 \sim 1037$  (cf. Fig. B3, top right, of this paper with Fig. 6d of

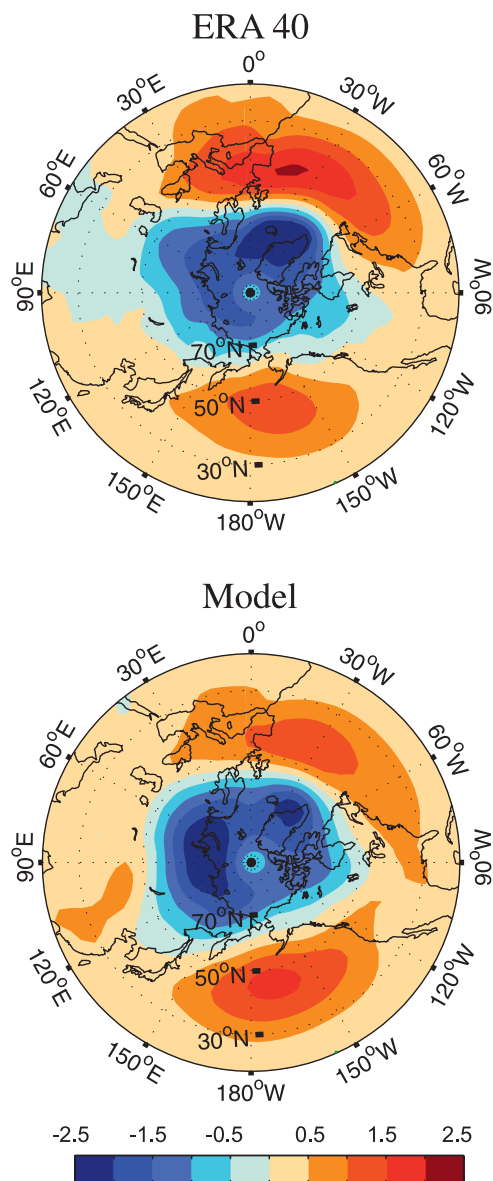


FIG. B4. Model simulation of Arctic Oscillation-like variability: the first EOF of the monthly sea level pressure anomaly north of  $20^{\circ}\text{N}$ , as obtained from (top) reanalysis (ERA-40) and (bottom) the model.

Gnanadesikan et al. 2006). Despite the lower ventilation rate, the bottom waters produced by CM2Mc circulate more vigorously throughout the global abyss (cf. Fig. B3, top panels, with Figs. 6c,d of Gnanadesikan et al. (2006)), consistent with observations, such as the strong bottom water flows recently observed near the Kerguelen Plateau (Fukamachi et al. 2010). The contrast in Southern Ocean ventilation appears to be due to a combination of the eddy parameterization (which enhances the eddy flux to high latitudes in CM2Mc, thereby abetting deep sinking), the altered freshwater discharge map (which allows higher nearshore salinities in CM2Mc), and the model grid. The supply of NADW to the deep ocean is very similar between the two models.

The Arctic Oscillation, based on the first leading mode of sea level pressure anomaly north of  $20^{\circ}\text{N}$ , is shown in Figure B4 for both the model and observations. Plots for the Southern Annular Mode and ENSO are given in the main text.

### c. Marine biogeochemical simulation

The marine biogeochemical tracers were integrated synchronously with the physical simulation for the latter half of the run (approximately 1000 years). The mean-state description here, and in section 2, pertains to the final 100 years of this run, while the discussion of variability includes the latter 500 years of the run.

The simulated  $\text{PO}_4$  field is fairly close to observations, especially considering the simplicity of the biogeochemical model and errors in the simulated ocean circulation. The principal features of the surface  $\text{PO}_4$  field are well captured (Fig. B5), including the very elevated Southern Ocean concentrations, low oligotrophic gyre concentrations, and elevated concentrations in low-latitude upwelling regions. We note that the high nutrient surface regions occur in the absence of explicit iron limitation.

The largest discrepancy versus observations occurs in the North Pacific where the surface nutrient concentration is dramatically lower than observed. This can be attributed to errors in the physical ocean circulation, such that nutrients are not maintained at intermediate depths where they can be resupplied to the surface (Fig. B5). A combination of the atmospheric simulation bias, poor resolution of topography near the Oyashio–Kuroshio confluence, and incorrect vertical mixing may be to blame. In contrast, the Atlantic meridional section shows  $\text{PO}_4$  concentrations that are close to the observations (Fig. B5).

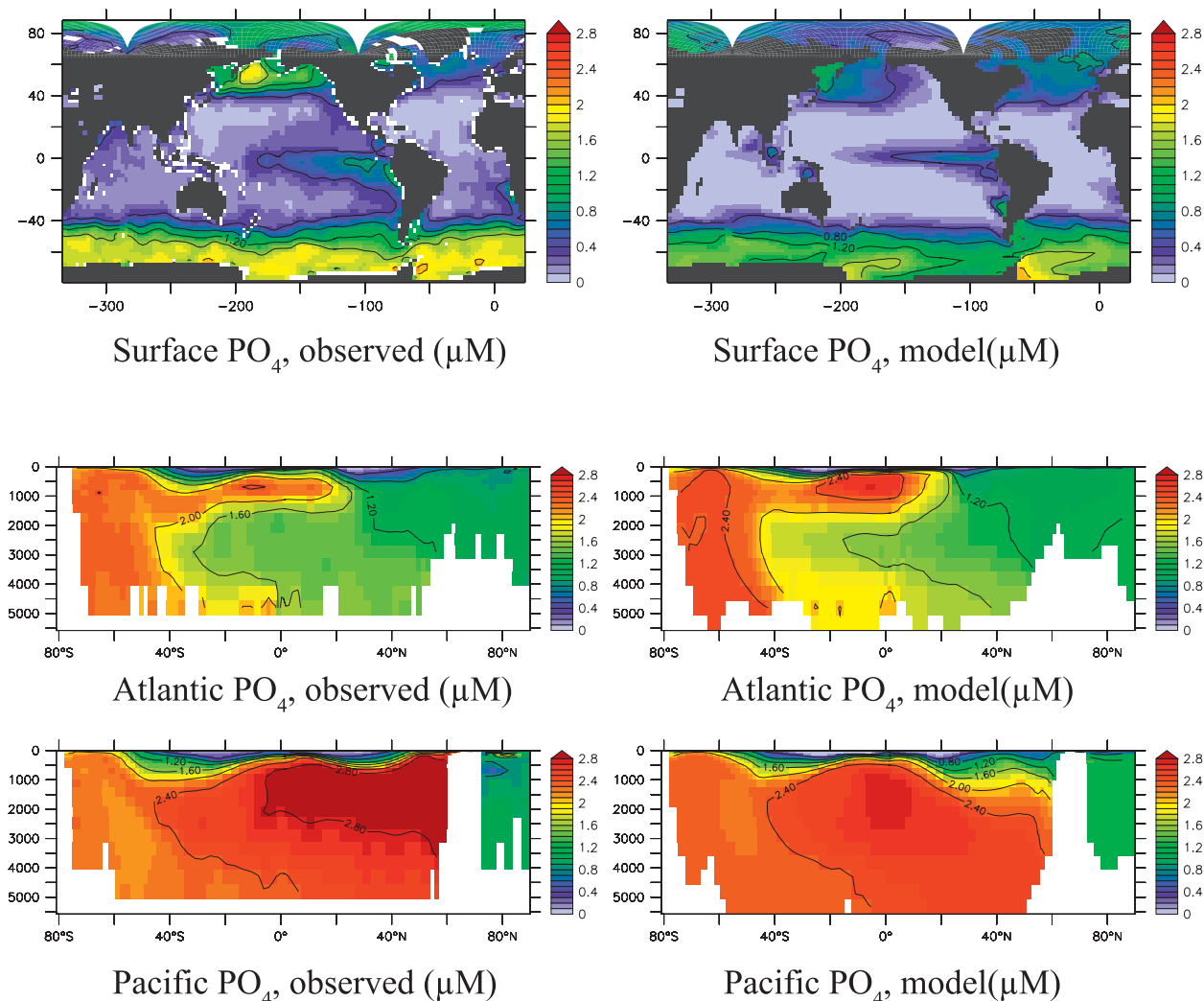


FIG. B5. Phosphate simulation of iBGC in CM2Mc: (left) observed phosphate concentrations (Conkright et al. 2002) and (right) model output for the (top) surface, (middle) zonal average between 30°W and 0° in the Atlantic Ocean, and (bottom) zonal average between 180° and 150°W in the Pacific Ocean.

#### REFERENCES

- Adcroft, A., C. Hill, and J. Marshall, 1997: Representation of topography by shaved cells in a height coordinate ocean model. *Mon. Wea. Rev.*, **125**, 2293–2315.
- , J. M. Campin, C. Hill, and J. Marshall, 2004: Implementation of an atmosphere–ocean general circulation model on the expanded spherical cube. *Mon. Wea. Rev.*, **132**, 2845–2863.
- Anderson, J. L., and Coauthors, 2004: The new GFDL global atmosphere and land model AM2-LM2: Evaluation with prescribed SST simulations. *J. Climate*, **17**, 4641–4673.
- Antonov, J. I., R. A. Locarnini, T. P. Boyer, A. V. Mishonov, and H. E. Garcia, 2006: *Salinity*. Vol. 2, *World Ocean Atlas 2005*, NOAA Atlas NESDIS 62, 182 pp.
- Bacastow, R., and E. Maier-Reimer, 1990: Ocean-circulation model of the carbon cycle. *Climate Dyn.*, **4**, 95–125.
- Bard, E., G. Raisbeck, F. Yiou, and J. Jouzel, 2000: Solar irradiance during the last 1200 years based on cosmogenic nuclides. *Tellus*, **52B**, 985–992.
- Böning, C. W., A. Dispert, M. Visbeck, S. R. Rintoul, and F. U. Schwarzkopf, 2008: The response of the Antarctic Circumpolar Current to recent climate change. *Nat. Geosci.*, **1**, 864–869.
- Broecker, W., and S. Barker, 2007: A 190 permil drop in atmosphere's  $\Delta 14\text{-C}$  during the “Mystery Interval” (17.5 to 14.5 kyr). *Earth Planet. Sci. Lett.*, **256**, 90–99.
- Carsey, F. D., 1980: Microwave observations of the Wedell Polynya. *Mon. Wea. Rev.*, **108**, 2031–2044.
- Collins, M., and Coauthors, 2010: The impact of global warming on the tropical Pacific and El Niño. *Nat. Geosci.*, **3**, 391–397.
- Conkright, M. E., R. A. Locarnini, H. E. Garcia, T. D. O’Brien, T. P. Boyer, C. Stephens, and J. I. Antonov, 2002: *World Ocean Atlas 2001: Objective Analysis, Data Statistics, and Figures*. National Oceanographic Data Center, CD-ROM.

- Cunningham, S. A., S. G. Alderson, B. A. King, and M. A. Brandon, 2003: Transport and variability of the Antarctic Circumpolar Current in Drake Passage. *J. Geophys. Res.*, **108**, 8084, doi:10.1029/2001JC001147.
- de Szoeke, S. P., and S. P. Xie, 2008: The tropical eastern Pacific seasonal cycle: Assessment of errors and mechanisms in IPCC AR4 coupled ocean-atmosphere general circulation models. *J. Climate*, **21**, 2573–2590.
- Delworth, T. L., and Coauthors, 2006: GFDL's CM2 global coupled climate models. Part I: Formulation and simulation characteristics. *J. Climate*, **19**, 643–674.
- Domack, E., A. Leventer, R. Dunbar, F. Taylor, S. Brachfeld, and C. Sjunneskog, 2001: Chronology of the Palmer Deep site, Antarctic Peninsula: A Holocene palaeoenvironmental reference for the circum-Antarctic. *Holocene*, **11**, 1–9.
- Druffel, E. R. M., 1997: Geochemistry of corals: Proxies of past ocean chemistry, ocean circulation, and climate. *Proc. Natl. Acad. Sci. USA*, **94**, 8354–8361.
- , S. Griffin, J. Hwang, T. Kimoda, S. R. Beaupre, K. C. Druffel-Rodriguez, G. M. Santos, and J. Southon, 2004: Variability of monthly radiocarbon during the 1760s in corals from the Galapagos Islands. *Radiocarbon*, **46**, 627–631.
- , —, S. R. Beaupre, and R. B. Dunbar, 2007: Oceanic climate and circulation changes during the past four centuries from radiocarbon in corals. *Geophys. Res. Lett.*, **34**, L09601, doi:10.1029/2006GL028681.
- Duffy, P. B., K. Caldeira, J. Selvaggi, and M. I. Hoffert, 1997: Effects of subgrid-scale mixing parameterizations on simulated distributions of natural C-14, temperature, and salinity in a three-dimensional ocean general circulation model. *J. Phys. Oceanogr.*, **27**, 498–523.
- Fallon, S. J., and T. P. Guilderson, 2008: Surface water processes in the Indonesian throughflow as documented by a high-resolution coral Delta C-14 record. *J. Geophys. Res.*, **113**, C09001, doi:10.1029/2008JC004722.
- Farnetti, R., T. L. Delworth, A. Rosati, S. Griffies, and F. Zeng, 2010: The role of mesoscale eddies in the rectification of the Southern Ocean response to climate change. *J. Phys. Oceanogr.*, **40**, 1539–1557.
- Fukamachi, Y., S. Rintoul, J. A. Church, K. Aoki, A. Sokolov, M. A. Rosenberg, and M. Wakatsuchi, 2010: Strong export of Antarctic Bottom Water east of the Kerguelen plateau. *Nat. Geosci.*, **3**, 327–331.
- Galbraith, E. D., S. L. Jaccard, T. F. Pedersen, D. M. Sigman, G. H. Haug, M. Cook, J. R. Southon, and R. Francois, 2007: Carbon dioxide release from the North Pacific abyss during the last deglaciation. *Nature*, **449**, 890–893.
- , A. Gnanadesikan, J. Dunne, and M. R. Hiscock, 2010: Regional impacts of iron-light colimitation in a global biogeochemical model. *Biogeosciences*, **7**, 1043–1064.
- Gent, P. R., and J. C. McWilliams, 1990: Isopycnal mixing in ocean circulation models. *J. Phys. Oceanogr.*, **20**, 150–155.
- Ginoux, P., L. W. Horowitz, V. Ramaswamy, I. V. Geogdzhayev, B. N. Holben, G. Stenchikov, and X. Tie, 2006: Evaluation of aerosol distribution and optical depth in the Geophysical Fluid Dynamics Laboratory coupled model CM2.1 for present climate. *J. Geophys. Res.*, **111**, D22210, doi:10.1029/2005JD006707.
- Gnanadesikan, A., J. P. Dunne, R. M. Key, K. Matsumoto, J. L. Sarmiento, R. D. Slater, and P. S. Swathi, 2004: Oceanic ventilation and biogeochemical cycling: Understanding the physical mechanisms that produce realistic distributions of tracers and productivity. *Global Biogeochem. Cycles*, **18**, GB4010, doi:10.1029/2003GB002097.
- , and Coauthors, 2006: GFDL's CM2 global coupled climate models. Part II: The baseline ocean simulation. *J. Climate*, **19**, 675–697.
- , S. M. Griffies, and B. L. Samuels, 2007: Effects in a climate model of slope tapering in neutral physics schemes. *Ocean Modell.*, **16**, 1–16.
- Gordon, A. L., M. Visbeck, and J. Comiso, 2007: A possible link between the Weddell Polynya and the Southern Annular Mode. *J. Climate*, **20**, 2558–2571.
- , R. D. Susanto, A. Ffield, B. A. Huber, W. Pranowo, and S. Wirasantosa, 2008: Makassar Strait throughflow, 2004 to 2006. *Geophys. Res. Lett.*, **35**, L24605, doi:10.1029/2008GL036372.
- Griffies, S. M., 2009: Elements of MOM4p1. GFDL Ocean Group Tech. Rep. 6, 444 pp.
- , and Coauthors, 2005: Formulation of an ocean model for global climate simulations. *Ocean Sci.*, **1**, 45–79.
- Grumet, N. S., P. B. Duffy, M. E. Wickett, K. Caldeira, and R. B. Dunbar, 2005: Intrabasin comparison of surface radiocarbon levels in the Indian Ocean between coral records and three-dimensional global ocean models. *Global Biogeochem. Cycles*, **19**, GB2010, doi:10.1029/2004GB002289.
- Guilderson, T. P., D. P. Schrag, M. Kashgarian, and J. Southon, 1998: Radiocarbon variability in the western equatorial Pacific inferred from a high-resolution coral record from Nauru Island. *J. Geophys. Res.*, **103**, 24 641–24 650.
- , K. Caldeira, and P. B. Duffy, 2000: Radiocarbon as a diagnostic tracer in ocean and carbon cycle modeling. *Global Biogeochem. Cycles*, **14**, 887–902.
- , S. Fallon, M. D. Moore, D. P. Schrag, and C. D. Charles, 2009: Seasonally resolved surface water  $\Delta^{14}\text{C}$  variability in the Lombok Strait: A coralline perspective. *J. Geophys. Res.*, **114**, C07029, doi:10.1029/2008JC004876.
- Guilyardi, E., A. Wittenberg, A. Fedorov, M. Collins, C. Wang, A. Capotondi, G. J. van Oldenborgh, and T. Stockdale, 2009: Understanding El Niño in ocean-atmosphere general circulation models: Progress and challenges. *Bull. Amer. Meteor. Soc.*, **90**, 325–340.
- Hall, A., and M. Visbeck, 2002: Synchronous variability in the Southern Hemisphere atmosphere, sea ice, and ocean resulting from the annular mode. *J. Climate*, **15**, 3043–3057.
- Haywood, J. M., V. Ramaswamy, and B. J. Soden, 1999: Tropospheric aerosol climate forcing in clear-sky satellite observations over the oceans. *Science*, **283**, 1299–1303.
- Hughen, K. A., J. T. Overpeck, S. J. Lehman, M. Kashgarian, J. Southon, L. C. Peterson, R. Alley, and D. M. Sigman, 1998: Deglacial changes in ocean circulation from an extended radiocarbon calibration. *Nature*, **391**, 65–68.
- , S. Lehman, J. Southon, J. Overpeck, O. Marchal, C. Herring, and J. Turnbull, 2004: C-14 activity and global carbon cycle changes over the past 50,000 years. *Science*, **303**, 202–207.
- Key, R. M., and Coauthors, 2004: A global ocean carbon climatology: Results from Global Data Analysis Project (GLODAP). *Global Biogeochem. Cycles*, **18**, GB4031, doi:10.1029/2004GB002247.
- Knudsen, M. F., P. Riisager, B. H. Jacobsen, R. Muscheler, I. Snowball, and M. S. Seidenkrantz, 2009: Taking the pulse of the Sun during the Holocene by joint analysis of C-14 and Be-10. *Geophys. Res. Lett.*, **36**, L16701, doi:10.1029/2009GL039439.
- Large, W. G., J. C. McWilliams, and S. C. Doney, 1994: Oceanic vertical mixing—A review and a model with a nonlocal boundary-layer parameterization. *Rev. Geophys.*, **32**, 363–403.
- , G. Danabasoglu, J. C. McWilliams, P. R. Gent, and F. O. Bryan, 2001: Equatorial circulation of a global ocean climate

- model with anisotropic horizontal viscosity. *J. Phys. Oceanogr.*, **31**, 518–536.
- Lee, H. C., A. Rosati, and M. J. Spelman, 2006: Barotropic tidal mixing effects in a coupled climate model: Oceanic conditions in the Northern Atlantic. *Ocean Modell.*, **11**, 464–477.
- Lin, S.-J., 2004: A “vertically Lagrangian” finite-volume dynamical core for global models. *Mon. Wea. Rev.*, **132**, 2293–2307.
- Locarnini, R. A., A. V. Mishonov, J. I. Antonov, T. P. Boyer, and H. E. Garcia, 2006: *Temperature*. Vol. 1, *World Ocean Atlas 2005*, NOAA Atlas NESDIS 61, 182 pp.
- Manizza, M., C. Le Quere, A. J. Watson, and E. T. Buitenhuis, 2005: Bio-optical feedbacks among phytoplankton, upper ocean physics and sea-ice in a global model. *Geophys. Res. Lett.*, **32**, L05603, doi:10.1029/2004GL020778.
- Mantua, N. J., S. R. Hare, Y. Zhang, J. M. Wallace, and R. C. Francis, 1997: A Pacific decadal climate oscillation with impacts on salmon. *Bull. Amer. Meteor. Soc.*, **78**, 1069–1079.
- Marchal, O., T. F. Stocker, F. Joos, A. Indermuhle, T. Blunier, and J. Tschumi, 1999: Modelling the concentration of atmospheric CO<sub>2</sub> during the Younger Dryas climate event. *Climate Dyn.*, **15**, 341–354.
- Marchitto, T., S. J. Lehman, J. D. Ortiz, J. Fluckiger, and A. van Geen, 2007: Marine radiocarbon evidence for the mechanism of deglacial atmospheric CO<sub>2</sub> rise. *Science*, **316**, 1456–1459.
- Marshall, G. J., 2002: Analysis of recent circulation and thermal advection change in the northern Antarctic Peninsula. *Int. J. Climatol.*, **22**, 1557–1567.
- Masarik, J., and J. Beer, 1999: Simulation of particle fluxes and cosmogenic nuclide production in the earth’s atmosphere. *J. Geophys. Res.*, **104**, 12 099–12 111.
- Matsumoto, K., and Coauthors, 2004: Evaluation of ocean carbon cycle models with data-based metrics. *Geophys. Res. Lett.*, **31**, L07303, doi:10.1029/2003GL018970.
- McCormac, F. G., A. G. Hogg, P. G. Blackwell, C. E. Buck, T. F. G. Higham, and P. J. Reimer, 2004: SHCal04 Southern Hemisphere calibration, 0–11.0 cal kyr BP. *Radiocarbon*, **46**, 1087–1092.
- Meissner, K. J., A. Schmittner, A. J. Weaver, and J. F. Adkins, 2003: Ventilation of the North Atlantic Ocean during the Last Glacial Maximum: A comparison between simulated and observed radiocarbon ages. *Paleoceanography*, **18**, 1023, doi:10.1029/2002PA000762.
- Milly, P. C. D., and A. B. Shmakin, 2002: Global modeling of land water and energy balances. Part I: The land dynamics (LaD) model. *J. Hydrometeorol.*, **3**, 283–299.
- Murray, R. J., 1996: Explicit generation of orthogonal grids for ocean models. *J. Comput. Phys.*, **126**, 251–273.
- Muscheler, R., F. Joos, J. Beer, S. A. Muller, M. Vonmoos, and I. Snowball, 2007: Solar activity during the last 1000 yr inferred from radionuclide records. *Quat. Sci. Rev.*, **26**, 82–97.
- Najjar, R., and J. C. Orr, cited 1998: Design of OCMIP-2 simulations of chlorofluorocarbons, the solubility pump and common biogeochemistry. [Available online at <http://www.cgd.ucar.edu/oce/OCMIP/design.pdf>.]
- Naveira Garabato, A. C., K. L. Polzin, B. A. King, K. J. Heywood, and M. Visbeck, 2004: Widespread intense turbulent mixing in the Southern Ocean. *Science*, **303**, 210–213.
- Pacanowski, R. C., and A. Gnanadesikan, 1998: Transient response in a z-level ocean model that resolves topography with partial cells. *Mon. Wea. Rev.*, **126**, 3248–3270.
- Redfield, A. C., B. H. Ketchum, and F. A. Richards, 1963: The influence of organisms on the composition of sea-water. *The Sea*, M. N. Hill, Ed., John Wiley & Sons, 26–77.
- Reimer, P. J., and Coauthors, 2004: IntCal04 terrestrial radiocarbon age calibration, 0–26 cal kyr BP. *Radiocarbon*, **46**, 1029–1058.
- Reynolds, R. W., N. A. Rayner, T. M. Smith, D. C. Stokes, and W. Wang, 2002: An improved in situ and satellite SST analysis for climate. *J. Climate*, **15**, 1609–1625.
- Rodgers, K. B., M. A. Cane, and D. P. Schrag, 1997: Seasonal variability of sea surface Delta C-14 in the equatorial Pacific in an ocean circulation model. *J. Geophys. Res.*, **102**, 18 627–18 639.
- , D. P. Schrag, M. A. Cane, and N. H. Naik, 2000: The bomb C-14 transient in the Pacific Ocean. *J. Geophys. Res.*, **105**, 8489–8512.
- , O. Aumont, G. Madec, C. Menkes, B. Blanke, P. Monfray, J. C. Orr, and D. P. Schrag, 2004: Radiocarbon as a thermocline proxy for the eastern equatorial Pacific. *Geophys. Res. Lett.*, **31**, L14314, doi:10.1029/2004GL019764.
- , and Coauthors, 2011: Interhemispheric gradient of atmospheric radiocarbon reveals natural variability of Southern Ocean winds. *Climate Past Discuss.*, **7**, 347–379.
- Rubin, S. I., and R. M. Key, 2002: Separating natural and bomb-produced radiocarbon in the ocean: The potential alkalinity method. *Global Biogeochem. Cycles*, **16**, 1105, doi:10.1029/2001GB001432.
- Schmittner, A., 2003: Southern Ocean sea ice and radiocarbon ages of glacial bottom waters. *Earth Planet. Sci. Lett.*, **213**, 53–62.
- Shackleton, N. J., J. C. Duplessy, M. Arnold, P. Maurice, M. A. Hall, and J. Cartlidge, 1988: Radiocarbon age of last glacial Pacific deep water. *Nature*, **335**, 708–711.
- Siegenthaler, U., M. Heimann, and H. Oeschger, 1980: C-14 variations caused by changes in the global carbon cycle. *Radiocarbon*, **22**, 177–191.
- Simmons, H. L., S. R. Jayne, L. C. St. Laurent, and A. J. Weaver, 2004: Tidally driven mixing in a numerical model of the ocean general circulation. *Ocean Modell.*, **6**, 245–263.
- Skinner, L. C., S. Fallon, C. Waelbroeck, E. Michel, and S. Barker, 2010: Ventilation of the deep Southern Ocean and deglacial CO<sub>2</sub> rise. *Science*, **328**, 1147–1151.
- Smethie, W. M., D. A. LeBel, R. A. Fine, M. Rhein, and D. Kieke, 2007: On past and future changes of the ocean’s meridional overturning circulation. *Past and Future Changes of the Ocean’s Meridional Overturning Circulation: Mechanisms and Impacts*, *Geophys. Monogr.*, Vol. 173, Amer. Geophys. Union, 119–130.
- Smith, R. D., and J. C. McWilliams, 2003: Anisotropic horizontal viscosity for ocean models. *Ocean Modell.*, **5**, 129–156.
- Stocker, T. F., and D. G. Wright, 1996: Rapid changes in ocean circulation and atmospheric radiocarbon. *Paleoceanography*, **11**, 773–795.
- Stuiver, M., and H. A. Polach, 1977: Reporting of <sup>14</sup>C data. *Radiocarbon*, **19**, 355–363.
- , and P. D. Quay, 1980: Changes in atmospheric C-14 attributed to a variable sun. *Science*, **207**, 11–19.
- Suess, E., 1953: Natural radiocarbon and the rate of exchange of carbon dioxide between the atmosphere and the sea. *Nuclear Processes in Geologic Settings*, National Research Council Committee on Nuclear Science, Ed., University of Chicago Press, 52–56.
- , 1968: *Climatic Changes, Solar Activity, and the Cosmic-Ray Production Rate of the Natural Radiocarbon*. *Meteor. Monogr.*, No. 8, Amer. Meteor. Soc., 146–150.
- Tillinger, D., and A. L. Gordon, 2009: Fifty years of the Indonesian Throughflow. *J. Climate*, **22**, 6342–6355.

- Toggweiler, J. R., and B. Samuels, 1993: New radiocarbon constraints on the upwelling of abyssal water to the ocean's surface. *The Global Carbon Cycle*, M. Heimann, Ed., Springer-Verlag, 333–365.
- , K. Dixon, and K. Bryan, 1989: Simulations of radiocarbon in a coarse-resolution world ocean model 1: Steady-state pre-bomb distributions. *J. Geophys. Res.*, **94**, 8217–8242.
- , —, and W. S. Broecker, 1991: The Peru upwelling and the ventilation of the South Pacific thermocline. *J. Geophys. Res.*, **96**, 20 467–20 497.
- , J. L. Russell, and S. R. Carson, 2006: Midlatitude westerlies, atmospheric CO<sub>2</sub>, and climate change during the ice ages. *Paleoceanography*, **21**, PA2005, doi:10.1029/2005PA001154.
- Vecchi, G. A., and A. T. Wittenberg, 2010: El Niño and our future climate: Where do we stand? *Wiley Interdiscip. Rev.: Climate Change*, **1**, 260–270.
- Visbeck, M., 2009: A station-based southern annular mode index from 1884 to 2005. *J. Climate*, **22**, 940–950.
- Wanninkhof, R., 1992: Relationship between wind-speed and gas-exchange over the ocean. *J. Geophys. Res.*, **97**, 7373–7382.
- Winton, M., and E. S. Sarachik, 1993: Thermohaline oscillations induced by strong steady salinity forcing of ocean general circulation models. *J. Phys. Oceanogr.*, **23**, 1389–1410.
- Wittenberg, A. T., 2009: Are historical records sufficient to constrain ENSO simulations? *Geophys. Res. Lett.*, **36**, L12702, doi:10.1029/2009GL038710.
- , A. Rosati, N. C. Lau, and J. J. Ploshay, 2006: GFDL's CM2 global coupled climate models. Part III: Tropical Pacific climate and ENSO. *J. Climate*, **19**, 698–722.
- Woodgate, R. A., and K. Aagaard, 2005: Revising the Bering Strait freshwater flux into the Arctic Ocean. *Geophys. Res. Lett.*, **32**, L02602, doi:10.1029/2004GL021747.